Graphical Abstract

Experimentally validated DEM for large deformation powder compaction: mechanically-derived contact model and screening of non-physical contacts

William Zunker, Sachith Dunatunga, Subhash Thakur, Pingjun Tang, Ken Kamrin

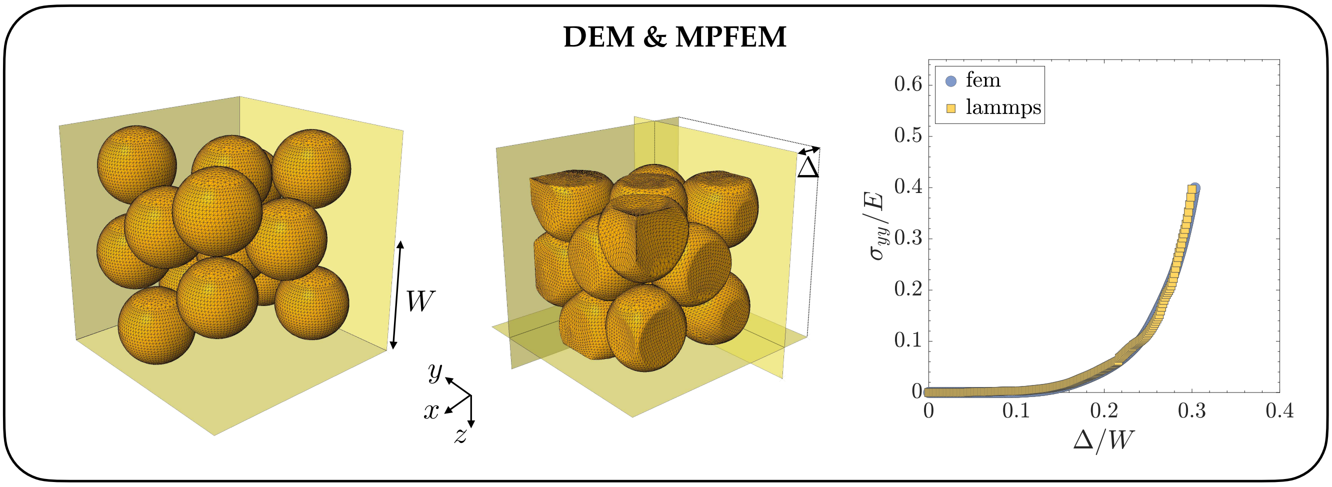

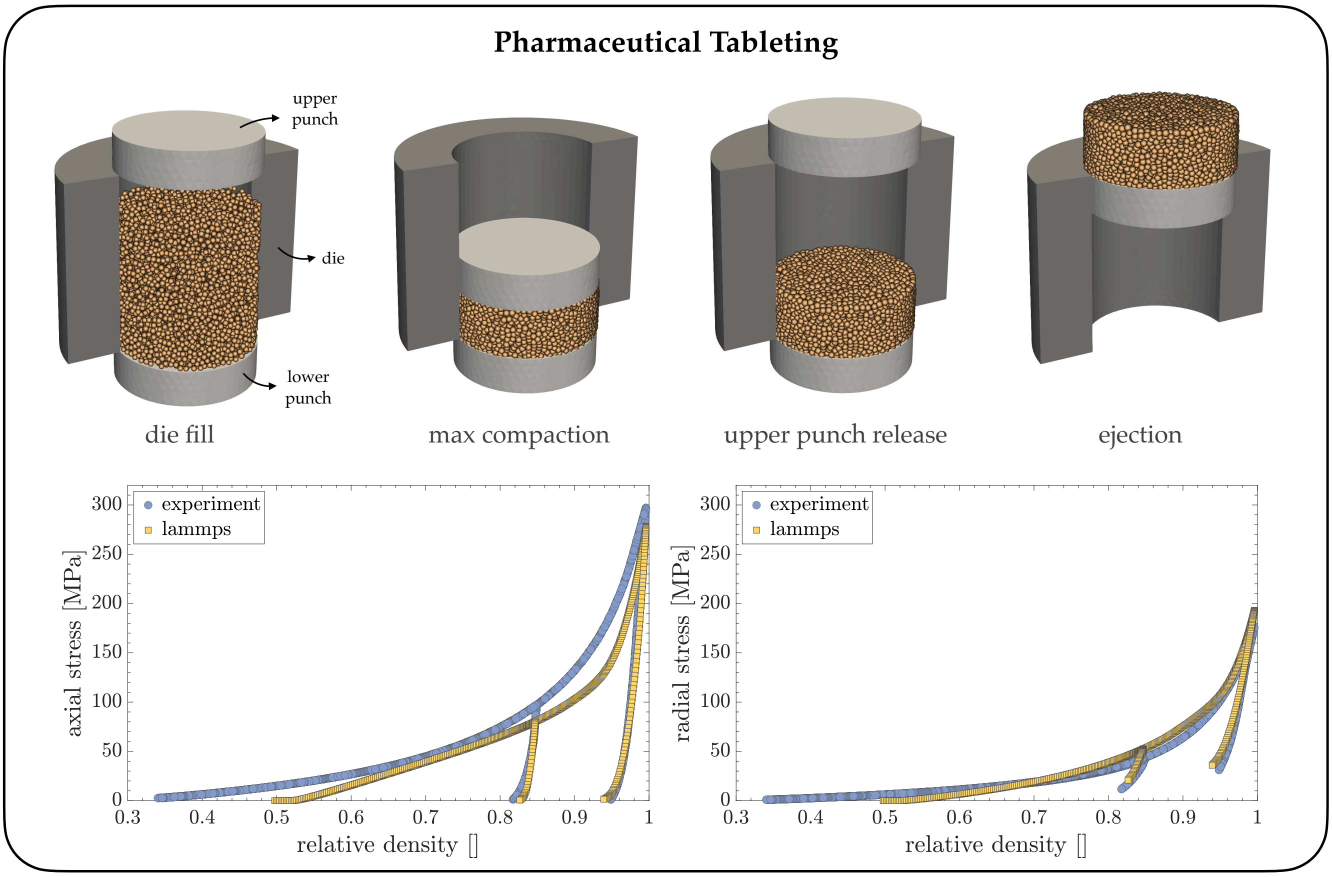

Highlights

Experimentally validated DEM for large deformation powder compaction: mechanically-derived contact model and screening of non-physical contacts

William Zunker, Sachith Dunatunga, Subhash Thakur, Pingjun Tang, Ken Kamrin

- Large deformation adhesive elastic-plastic powder compaction is studied.

- A recently proposed adhesive elastic-plastic contact model is further developed.

- A new algorithm screens non-physical contacts in large deformation DEM simulations.

- The extended contact model is implemented in LAMMPS and validated with MPFEM.

- Pharmaceutical tableting simulations show strong agreement with experimental data.

Experimentally validated DEM for large deformation powder compaction: mechanically-derived contact model and screening of non-physical contacts

William Zunker[a], Sachith Dunatunga[a], Subhash Thakur[c], Pingjun Tang[c], Ken Kamrin[a,b,*]

[a] *Department of Mechanical Engineering, Massachusetts Institute of Technology, 77 Massachusetts Ave, Cambridge, 02319, MA, USA*
[b] *Department of Mechanical Engineering, University of California Berkeley, University Ave, Berkeley, 94720, CA, USA*
[c] *Vertex Pharmaceuticals, 50 Northern Avenue, Boston, 02210, MA, USA*

Abstract

Despite widespread industrial reliance on powder compaction in manufacturing, a complete understanding of the underlying physical mechanisms that lead to pore structure, mechanical strength, and defects remains elusive, challenging ongoing efforts to optimize the process and improve product quality. The discrete element method (DEM) is a promising tool for studying powder compaction due to its algorithmic simplicity and particle-level insights, but its application is limited by the lack of accessible, physically justified contact models for large deformations. In this work, we help address this problem by extending the recently proposed mechanically-derived adhesive elastic-plastic contact model [1, 2] suitable for large deformation to the case of many-interacting particles. A topological penalty algorithm for the screening of non-physical contacts occurring through obstructing particles, a phenomenon unique to large deformation DEM, is also proposed. The extended version of the contact model and topological penalty algorithm are implemented into the open-source DEM software LAMMPS (https://github.com/lammps/lammps) and validated against the multi-particle finite element method (MPFEM). The contact model's unique ability to reconstruct deformed particle shapes is highlighted by comparison to FEM predictions. The industrially relevant problem of pharmaceutical tableting is simulated and comparisons to experimental data for the compaction of Avicel PH102 (microcrystalline cellulose) are made. Good agreement is observed between the experiment and numerical simulation for the axial and radial stress measurements as a function of relative density. Notably, the simulation is able to predict a similar residual radial stress after release of the axially confining pressure to that of the experiment.

Keywords: discrete element method, large deformation powder compaction, tableting, adhesive elastic-plastic, multi-particle finite element method, normal contact model

---

1. Introduction

Compaction of powders is a common manufacturing process in many sectors. It is used in automotive [3, 4], aerospace [5, 6], and ceramics [7] applications to produce complex and durable components typically intended for extended use under heavy cyclic loading. Pharmaceutical [8, 9] and consumer goods [10], on the other hand, use it to create single-use products such as tablets or detergent pellets that will be exposed to markedly different conditions including biologic or aqueous environments. Electrode calendaring in battery manufacturing [11, 12] represents yet another unique application, in which dried, powder-based electrodes are compacted to enhance energy density, improve electrical contact, and ensure mechanical stability. Regardless of the application, the objective of powder compaction is the same: produce a dense defect-free compact with precisely controlled porosity and mechanical strength [13]. Although the goal is well-defined, complications often arise that can lead to defects and other undesirable outcomes [14, 15, 16, 17, 18]. Many of these issues stem from the extreme pressures that are applied to the powders which lead to significant particle rearrangement [19, 20], inelastic deformation [21], adhesive bonding [22], and coupled interaction with another phase such as air [23] or water [24]. Due to the widespread industrial relevance of powder compaction, parsing this rich set of entangled physics is crucial to improving our understanding of the process.

Although experimentation is the primary technique used in industrial settings to refine powder manufacturing processes, numerical simulation has been growing in favor in recent years. The reliance on both techniques is due to their complementary nature. Experimentation offers direct, but often macroscopic, characterization of the exact powder (blend) of interest during compaction. In contrast, simulation provides full-field or even per-particle information of various physical quantities at all stages of compaction, but for an idealized version of the powder (blend) of interest. However, the process of idealizing the powder to only include the essential physics is what endows numerical simulation with the ability to isolate and begin to untangle different physical mechanisms that lead to various properties of compacts.

Three popular numerical approaches to modeling powder compaction are continuum modeling, the multi-particle finite

---

[*] Corresponding author.
Email address: `kkamrin@berkeley.edu` (Ken Kamrin)

element method (MPFEM), and the discrete element method (DEM). Oftentimes, the techniques are used in tandem in investigations [25, 26] since they each provide unique advantages and have their own set of limitations.

Continuum modeling has been employed to understand a variety of powder compaction applications from cold compaction of metal powders [27, 28] to pharmaceutical tableting [29, 30, 31]. The homogenization of the powder into a continuous media allows for efficient simulation of arbitrarily large systems that would be computationally intractable with MPFEM or DEM. Accuracy of continuum simulations relies on precise formulation of the constitutive relation, however there is still no generally accepted constitutive relation for cohesive powders that can be calibrated robustly and easily to different powder grains [32]. This, combined with the inability of continuum formulations to capture particle-level properties such as size, size distribution, pore structure, or spatial configuration of particles limits the applicability of continuum methods, especially for prediction of defects [14].

MPFEM, first introduced by Gethin et al., [33], blends the benefits of continuum modeling and DEM. Like DEM, MPFEM represents the powder as discrete particles whose interaction is governed by defined contact laws. Unlike traditional DEM however, each particle is a fully meshed continuum body with a potentially unique prescribed material behavior. This endows MPFEM with the ability to accurately model the interaction of complex particle shapes such as hollow spheres [34], multi-material compaction [35], and adhesive bonding between materials taking into account large plastic deformations [36, 37]. The largest disadvantage of MPFEM is the severely increased computational cost for the same system size as compared to continuum modeling or even DEM. This limits the applicability to often unrealistic system sizes compared to industrial applications. Despite this, MPFEM is indispensable in calibration of DEM contact laws [38] and constitutive relations [39, 40].

Since its inception in 1979 by Cundall and Strack [41], DEM has grown in popularity and is commonly used to simulate powder behavior. It models each particle as a discrete object like MPFEM, however it utilizes simple, often analytic, contact models to determine contact forces that dictate the evolution of the system through integration of Newton's equations of motion. This places DEM's computational efficiency between that of continuum modeling and MPFEM, allowing certain industrial applications involving small amounts of powders to be directly simulated [42]. Due to the discrete nature of DEM it, like MPFEM, allows insight into the aforementioned microscopic particle-level properties missed by continuum methods. This makes DEM an attractive method to understand powder compaction, providing a balance between particle-level resolution and computational efficiency.

The crux of using DEM to model powder compaction has historically been the lack of a reliable normal contact model to capture adhesive elastic-plastic effects in a physically justified way. This is inherently a difficult task as the force-displacement relation for a contacting pair of adhesive elastic-plastic particles in a larger packing is riddled with complexities [43, 44, 45]. For a detailed overview of past adhesive elastic-plastic normal contact models and their relevant features see [1]. Recently, however, a new mechanically-derived contact model suitable for large deformation adhesive elastic perfectly-plastic contact, known as the method of dimensionality reduction (MDR) contact model, was introduced [1, 2]. It was shown to capture the essential features of the force-displacement relation in all contact regimes for a broad range of particle material behavior from rigid-plastic to fully-elastic. Despite the promising predictive capability, only simple symmetric loadings involving a single initially spherical particle and rigid flats were considered in the originally published works. *It is the intent of this paper to extend the MDR contact model to the many-interacting particle case and demonstrate its ability to model industrially relevant powder compaction processes. The purpose is to provide a flexible and reliable numerical tool that can assist in the process of relating underlying physical mechanisms to important compact properties like porosity, mechanical strength, and defects.*

In Section 2, the important features of the MDR contact model are reviewed and then it is extended to the many-interacting particle case, allowing implementation into the DEM software LAMMPS for open-source usage. Special contact force evaluation considerations for large deformation DEM will be discussed in Section 3. MPFEM will be employed as a ground truth validation of the many-interacting MDR contact model implementation in Section 4. A brief interlude will be taken in Section 5 to highlight the MDR contact model's unique capability to reconstruct deformed particle shapes and predict contact-level properties with comparison against FEM predictions. The paper will close with a description of pharmaceutical tablet compaction experiments and subsequent numerical simulation comparisons in Sections 6 and 7, respectively.

2. The MDR contact model, extension to many-interacting particles, and numerical implementation

2.1. Review of the MDR contact model

The MDR contact model derives its name from the powerful contact modeling technique that it is built upon: the method of dimensionality reduction (MDR) [46, 47]. This method allows the exact mapping of specific 3D contact problems to a corresponding simplified problem of a 1D plane rigid indenter contacting a bed of independent Hookean springs. Importantly, the force, displacement, and contact radius relations are preserved exactly between the two spaces, making the MDR an ideal candidate for the basis of a DEM contact model. Using the MDR as a foundation, the MDR contact model was developed which is described in detail in Appendix A. It has a number of important features to capture the contact response of adhesive elastic-plastic particles:

1. Analytical mechanically-derived formulation that is computationally cheap to evaluate based on the MDR.
2. The inputs to the model are primarily physical material properties: Young's modulus, Poisson's ratio, yield stress, and effective surface energy. The exception is the critical confinement ratio which determines when a specific bulk

elastic response will trigger, however this is still physically motivated and based on evaluation of the ratio of remaining free surface area not involved in contacts to the total free surface area[1].

3. Treats all three regimes: elastic, fully plastic, and bulk elastic with the correct unloading behaviors in each.
4. Includes a JKR type (fracture mechanics based) adhesion [48], enabled directly by the MDR framework, that is valid into large deformation.
5. Respects the incompressibility of plastic deformation and allows for definition of an apparent radius that captures free surface displacement induced by all particle contacts. This leads to capturing multi-neighbor dependent effects such as increased force at existing contacts and formation of new contacts caused by radial expansion.
6. The tracking of state variables allows reconstruction of not only force-displacement, but also each particle's plastically deformed shape, volume, contact areas, and contact pressure distributions.

The culmination of all these features leads to a robust contact model capable of handling the complexities of adhesive elastic-plastic contact in an efficient manner suitable for implementation into DEM.

2.2. *Extension to many-interacting particles*

Industrially relevant powder compaction processes such as pharmaceutical tableting often involves multi-component formulations that span a large range of particle size and material behavior [22]. In the development of the MDR contact model, only simple symmetric loadings involving rigid flats and a single initially spherical particle were considered. Conversion between these loading conditions and special cases of particle-particle contact can be made, however a more generic loading capability for the case of many-interacting particles with varying radii and material properties is desirable. Here, we focus on developing and testing a many-interacting particle methodology that properly handles varying radii, leaving the additional task of considering varying material properties as future work.

In developing the methodology for the many-interacting case, the objective is to alter the existing formulation of the MDR contact model minimally. To this end, we extend the idea of an isolated particle surrounded by rigid flats to the many-interacting particle case. To demonstrate this procedure, consider the interaction between particles i, j, k, and l all with distinct radii shown in Fig. 1. To determine the contact force at each pair of particles a simple procedure is followed:

1. Rigid flats are placed according to the rigid flat placement scheme described in Section 2.2.1.
2. The force on either side is calculated assuming interaction with a rigid flat. For example, for pair $\{i, k\}$ two forces will be calculated: F_{ik}^{k} and F_{ik}^{i}. The former is the force between particle k and the imagined rigid flat ignoring the presence of i. The latter is the force between particle i and that same imagined rigid flat ignoring the presence of k.
3. The forces on either side of the rigid flat are averaged to determine the final force for the contacting pair: $F_{ik} = (F_{ik}^{i} + F_{ik}^{k})/2$.

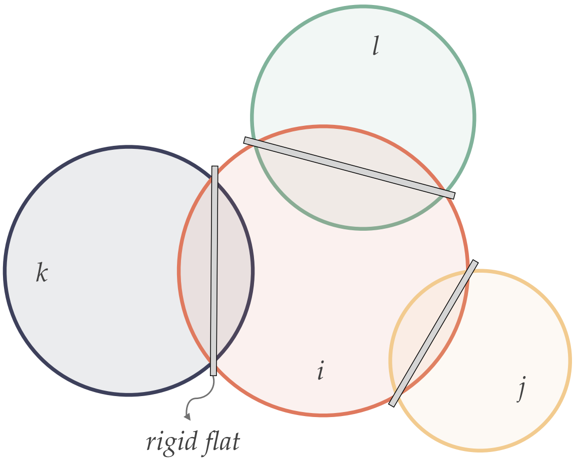

Figure 1: Many-interacting case between particles i, j, k, and l. Imagined rigid flats are placed at each contact.

This many-interacting methodology has the advantage that the MDR contact model formulation can be applied directly without adjustment in the presence of varying particle sizes. The trade-offs are: (i) computational efficiency is decreased due to the double force evaluation for each pair and (ii) there is possibility of contact property (e.g. area) discrepancy across a rigid flat for a contacting pair. Nevertheless, the methodology produces a unique force at each contact that results in a reasonable physical response as demonstrated in the upcoming sections.

2.2.1. *Rigid flat placement scheme*

Fig. 2a shows a contact between particles i and j with apparent radii R_i and R_j, respectively. The apparent overlap between the two particles is denoted by δ. The objective of the rigid flat placement scheme is to determine how to partition δ into apparent overlaps δ_i and δ_j for each respective particle (i.e., $\delta = \delta_i + \delta_j$).

We present a scheme that consists of two contributions: (i) a geometrically motivated placement during forward loading and (ii) a linear interpolation during unloading that ensures both sides of the contact unload to zero force simultaneously based on the knowledge of the plastic surface displacements. This results in the following expressions for the apparent overlaps

$$\delta_i = \delta_{\text{i,geo}}^{\max} - \frac{\delta_i^p - \delta_{\text{i,geo}}^{\max}}{\delta^p - \delta_{\max}}(\delta - \delta_{\max}), \tag{1}$$

$$\delta_j = \delta_{\text{j,geo}}^{\max} - \frac{\delta_j^p - \delta_{\text{j,geo}}^{\max}}{\delta^p - \delta_{\max}}(\delta - \delta_{\max}), \tag{2}$$

where $\delta_{\text{i,geo}}^{\max}$ and $\delta_{\text{j,geo}}^{\max}$ are the maximum experienced geometric apparent overlaps; δ_i^p and δ_j^p are the plastic displacements;

---

[1] For additional information on the critical confinement ratio and the related bulk elastic regime please see Appendix A

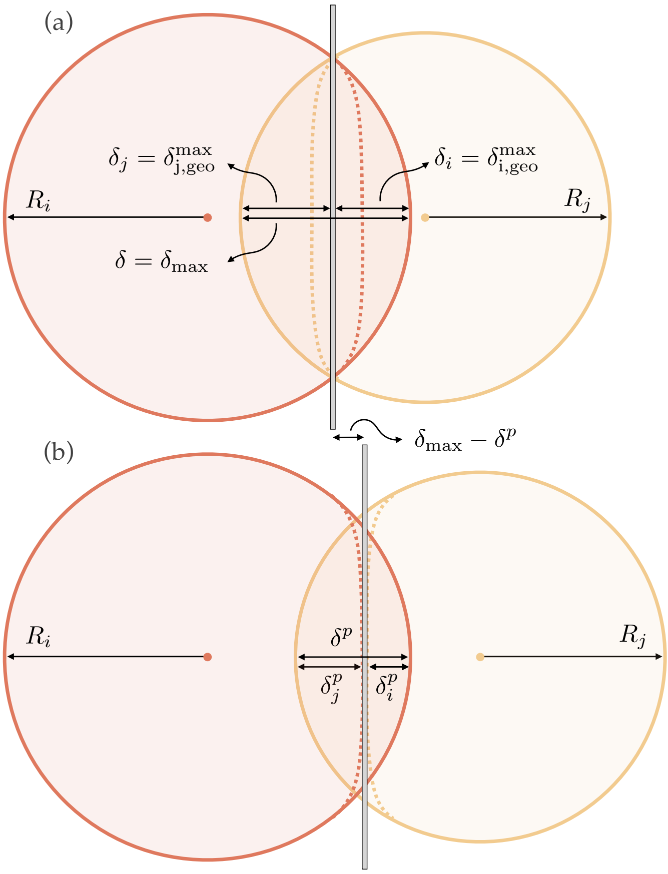

Figure 2: Kinematic and geometric quantities relevant to the rigid flat placement scheme for contact between particles *i* and *j*. (a) Maximum displacement step where the rigid flat is placed at the geometric intersection of $\{i, j\}$. The dashed lines represent the unloaded plastically deformed profiles. (b) During unloading the rigid flat placement scheme linearly interpolates the rigid flat placement through the state shown to reach zero force based on knowledge of the plastic displacements.

$\delta^p = \delta^p_i + \delta^p_j$ is the total plastic displacement; and $\delta_{\max}$ is the maximum experienced overlap.

To understand the two contributions we first consider the case of forward loading, characterized by $\delta = \delta_{\max}$, shown in Fig. 2a. Given that $\delta = \delta_{\max}$, expressions (1) and (2) reduce to only the first terms where

$$\delta^{\max}_{\mathrm{i,geo}} = \frac{\delta^2_{\max} - 2R_j\delta_{\max}}{2(\delta_{\max} - R_i - R_j)}, \tag{3}$$

$$\delta^{\max}_{\mathrm{j,geo}} = \frac{\delta^2_{\max} - 2R_i\delta_{\max}}{2(\delta_{\max} - R_i - R_j)}. \tag{4}$$

The scheme during forward loading is therefore guided by placement of the rigid flat at the geometric intersection between the two apparent radii. The justification for this placement comes from attempting to approximately match contact areas on either side of the rigid flat. This is motivated by a fundamental finding during the development of the MDR contact model that the contact area could be approximated from the geometric intersection in the fully plastic regime of contact. Under cases of extreme overlap as $\delta/R \rightarrow 1$ a slight adjustment of (3) and (4) is introduced to avoid non-physical placement of the rigid flat, this situation is discussed in Appendix B.

During unloading the second terms in (1) and (2) become nonzero. The purpose of these terms is to linearly interpolate the placement of the rigid flat during the unloading of $\{i, j\}$ such that both sides of the contact reach zero force simultaneously. This coincides with placing the rigid flat at the location where the deformed profiles touch as seen in Fig. 2b.

Validation of this rigid flat placement scheme for contacting particles of varying radii is given in Appendix C.

2.3. LAMMPS numerical implementation

The extended MDR contact model and the topological penalty algorithm described in the following section are formally implemented into the main repository of the open-source DEM software LAMMPS https://github.com/lammps/lammps. The most up-to-date version of the implementation is maintained on the *develop* branch of the repository. Information on the usage of the MDR model can be found in the LAMMPS documentation.

3. Screening of non-physical contacts for large deformation DEM

In typical DEM simulations a neighborhood algorithm [49, 50, 51] is used to find groups of neighboring particles that have the potential for contacting during a given step. Once grouped, contact is determined by a simple calculation: if two particles geometrically overlap, a non-zero force will be calculated. In DEM simulations involving small deformations this geometric overlap contact detection works well given that distinct contacts don't typically infringe on one another due to the overlap being small compared to the particle radii.

In large deformation DEM the situation changes dramatically as exemplified by Fig. 3a. Here, particles *i*, *j*, and *k* are subject to uniaxial compression between two rigid flats. The compression in this instance is large and has caused significant overlaps to develop between $\{i, k\}$, $\{j, k\}$, and $\{i, j\}$. The interesting question that arises from this large deformation is the following:

- Should particle *i* be able to contact *j* given the presence of *k*?

If we consider the deformation of the particles as shown in Fig. 3b, we clearly see that no contact between *i* and *j* should develop. However, in standard DEM a non-zero force will be evaluated for $\{i, j\}$ based on the geometric overlap.

A second example of this effect can be seen in Fig. 3c, where particles *i*, *j*, *k*, and *l* are subject to a uniform compression by rigid flats. We can again pose a similar question:

- Should particle *i* be able to contact *j* given the presence of *k* and *l*?

Inspection of Fig. 3d shows that when considering the deformation of the particles no contact between *i* and *j* should develop. In spite of this, a non-zero force would be evaluated in standard

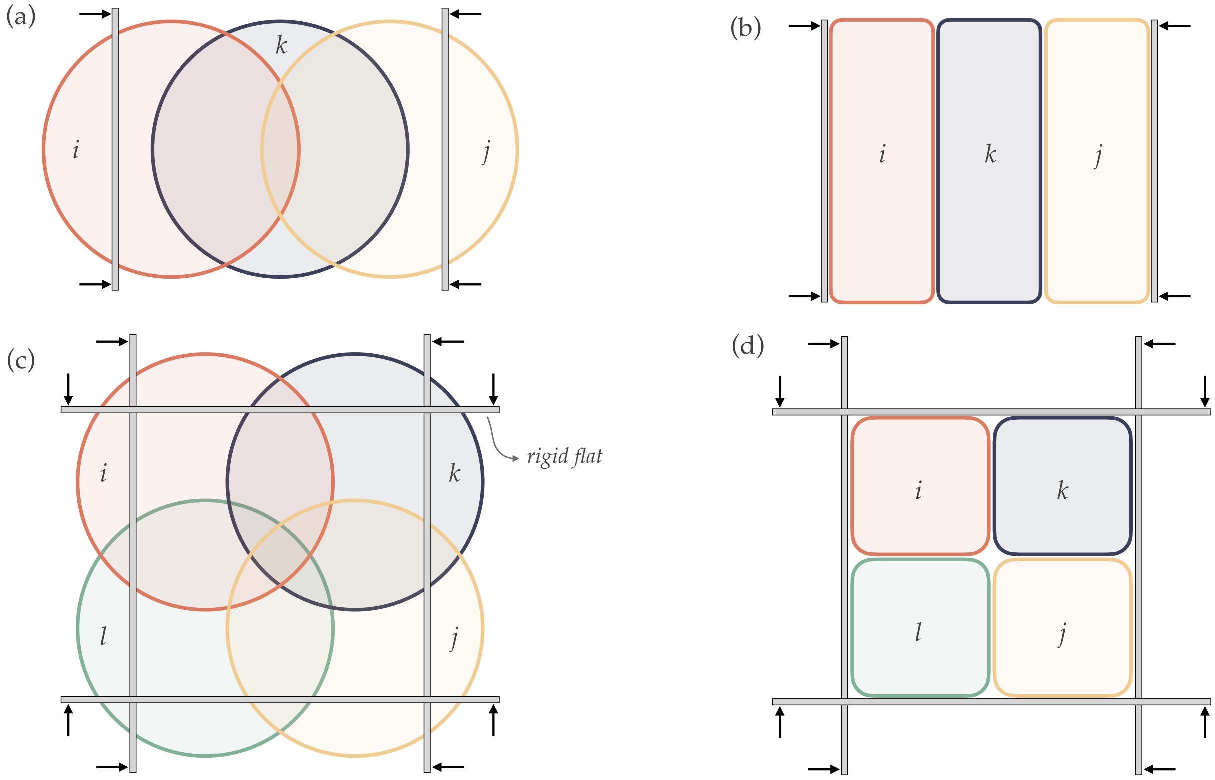

Figure 3: Two examples highlighting the special contact force evaluation considerations needed for large deformation DEM. (a) Uniaxial compression of three particles i, j, and k. (b) Visualization of the deformed particles induced by uniaxial compression. (c) Uniform compression of four particles i, j, k, and l. (d) Visualization of the deformed particles induced by uniform compression.

DEM due to the geometric overlap between $\{i, j\}$. An identical issue exists for the pair $\{k, l\}$ in this instance as well.

The two loadings of Fig. 3 highlight the shortcomings of relying solely on geometric overlap for contact detection and subsequent force evaluation in large deformation. This motivates the need to develop a more robust contact force evaluation screening process that avoids including non-physical contacts occurring through obstructing particles.

3.1. Topological penalty algorithm

The methodology behind the proposed additional screening of contact force evaluations during large deformation DEM relies on assigning penalties p to non-physical contacts occurring through obstructing particles. The penalty is designed to grow based on increasing obstruction of a contact by other particles. Once calculated, the penalty is converted into a weight w that is multiplied by the evaluated force F at a given contact. The range for the weight is $w \in [0, 1]$, meaning that the force may either be entirely negated, partially reduced, or unaltered. This scheme can be appended to any typical DEM code without introducing significant modification given that it only alters the final resulting force in the case of large overlaps.

To understand the process for calculating contact penalties consider the triplet of particles i, j, and k shown in Fig. 4. The topological penalty scheme consists of three steps: (i) check if penalization is necessary, (ii) calculate the penalty for the non-central contact, and (iii) calculate contact weights.

Check if penalization is necessary

The first step of the scheme involves checking if all three particles overlap with one another. If

$$\delta_{ij} \leq 0 \quad \text{or} \quad \delta_{ik} \leq 0 \quad \text{or} \quad \delta_{jk} \leq 0, \tag{5}$$

then all penalties are zero

$$p_{ij} = 0, \quad p_{ik} = 0, \quad p_{jk} = 0, \tag{6}$$

and the scheme avoids evaluating any penalties for that triplet. Fig. 4a is a situation in which $\delta_{ij} < 0$, meaning all penalties are automatically zero. Fig. 4b, on the other hand, is a case where all overlaps are positive meaning it is necessary to proceed to the penalty calculation.

Calculate the penalty for the non-central contact

The non-zero penalty for the triplet is assigned to the non-central particle contact. Non-centrality is determined by a simple distance metric where the three distances d between particle centers are run through a max function

$$\max(d_{ij}, d_{ik}, d_{jk}) = d_{ij}. \tag{7}$$

The missing subscript of the distance function, in this case k for Fig. 4b, indicates which particle is central based on the shortest distance between the other two particle centers. Two unit normal vectors $\boldsymbol{e}_{ki}$ and $\boldsymbol{e}_{kj}$ are defined, originating from the central particle and oriented towards the other particle centers. A dot

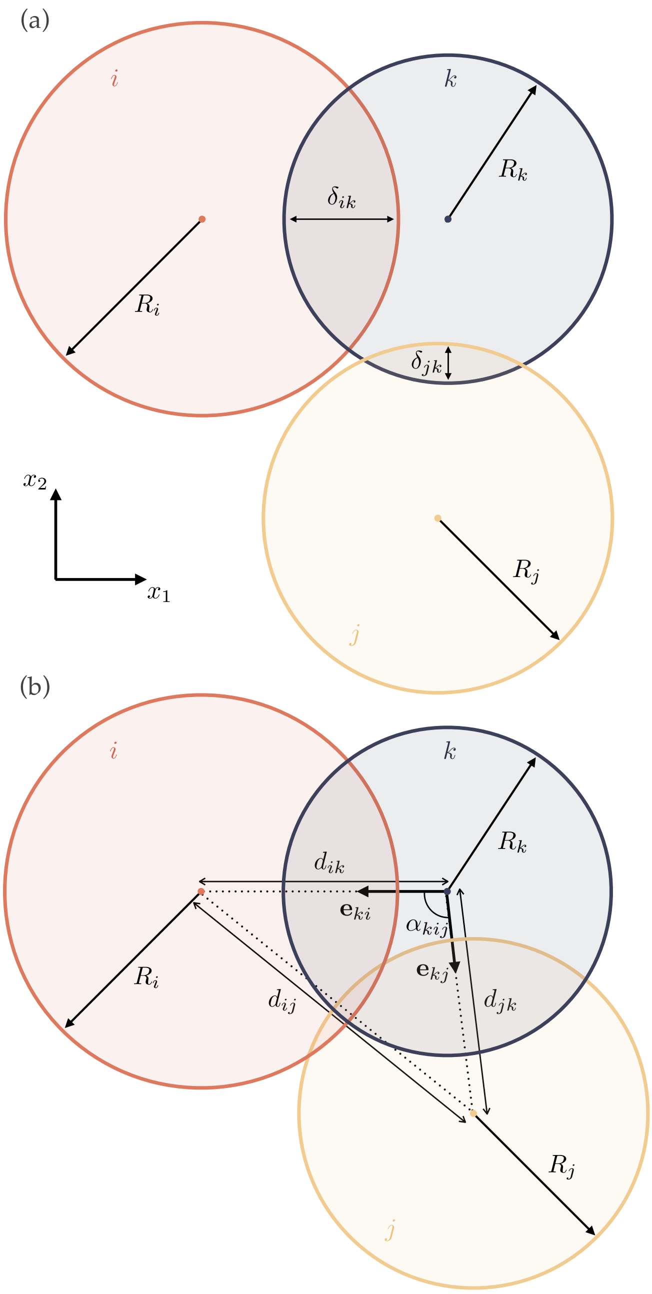

Figure 4: Triplet of particles i, j, and k under consideration for penalization: (a) no penalization is necessary and (b) penalization required for contact $\{i, j\}$.

product is calculated to determine the angle between the two unit vectors

$$\alpha_{kij} = \arccos\left(\boldsymbol{e}_{ki} \cdot \boldsymbol{e}_{kj}\right). \tag{8}$$

The penalties can then be calculated as follows: the non-central contact is assigned a penalty based on a sigmoid penalty function

$$\hat{p}(\alpha) = \frac{1}{1 + \exp\left(-t_p \frac{\alpha}{\pi} - \frac{1}{2}\right)}, \tag{9}$$

and the two other contacts receive zero penalty. In (9), t_p is a fitted penalty transition intensity, for all simulations conducted in this work $t_p = 50$. In the case under consideration the penalties are

$$p_{ij} = \hat{p}(\alpha_{kij}), \quad p_{ik} = 0, \quad p_{jk} = 0. \tag{10}$$

The first two steps, checking if penalization is necessary and calculating the penalty for the non-central contact, are repeated for all eligible neighboring triplets in the system. Triplet eligibility is determined strictly by the current neighbor lists of particles, this helps reduce computation time from evaluating triplets that clearly won't satisfy condition (5). In larger systems it is possible that a given contact may be considered non-central in multiple triplets. In this situation, the penalties incurred from each triplet are superimposed, *meaning a particular contact may be penalized multiple times if numerous neighboring particles all obstruct the contact.* An example of superimposed penalties is given in Appendix D.

Calculate contact weights

The final step involves converting the calculated penalties into weights. If we imagine our system to be restricted to only the triplet in Fig. 4b then only three weights need to be calculated

$$\begin{aligned} w_{ij} &= \max(1 - p_{ij}, 0), \\ w_{ik} &= \max(1 - p_{ik}, 0), \\ w_{jk} &= \max(1 - p_{jk}, 0). \end{aligned} \tag{11}$$

For larger systems individual weights need to be calculated for each active contact. These weights are then multiplied by the evaluated force to determine the final force at a given contact.

Extended discussion of the topological penalty scheme, including simple examples of weight calculations for a triplet experiencing a predominately shearing-type motion and justification of the selection of the sigmoid penalty function (9) can be found in Appendix D.

4. Multi-particle finite element method comparison

The MDR contact model was validated against FEM simulations involving an initially spherical single elastic-perfectly plastic particle compressed between rigid flats. All loadings considered were highly symmetric, leaving the case of many-interacting particles unexplored. To establish a ground truth dataset for the case of many-interacting particles, we turn to the multi-particle finite element method (MPFEM) [52, 53, 35, 40, 54, 55].

We define two simulations in Abaqus involving a handful of meshed initially spherical elastic-perfectly plastic particles being compressed between six rigid flats. The material properties assigned to the particle are $E/Y = 20$ and $\nu = 0.3$, where E/Y is the ratio between the Young's modulus and yield stress and ν is the Poisson's ratio. Kinematic control is enforced on the rigid flats displacing them equally towards the box center by a distance Δ. In both simulations, the interaction between particles and particle-walls is defined as hard contact in the normal direction and frictional in the tangential direction with a coefficient of 0.5. For the mesh, 10-node modified quadratic tetrahedron elements C3D10M are used. No damping is defined and both simulations are solved in Abaqus dynamic explicit. The

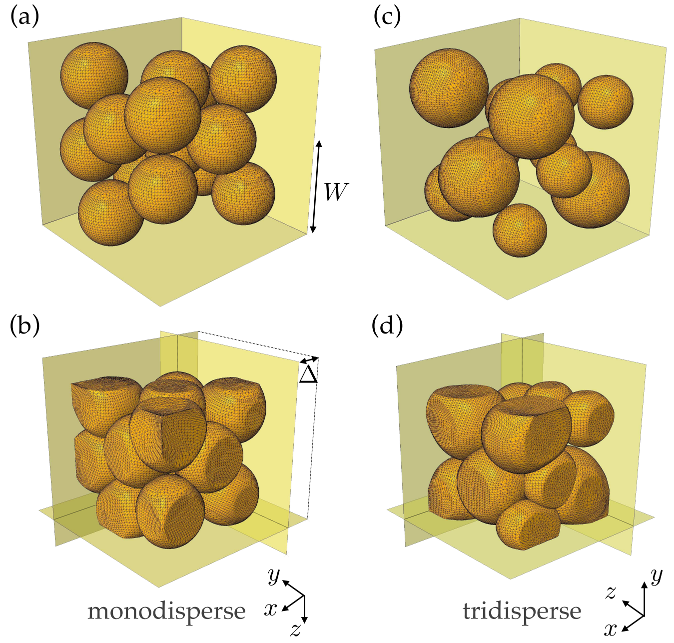

Figure 5: MPFEM results. Monodisperse (a) initial and (b) final deformed configuration. Tridisperse (c) initial and (d) final deformed configuration.

difference between the two simulations is in the distribution of particle radii. Fig. 5a and b show the compaction of fourteen monodisperse particles, whereas Fig. 5c and d show the compaction of twelve tridisperse particles. For the tridisperse case there are six small, two medium, and four large particles, where the descriptors small, medium, and large correspond to the relative particle diameters. Moving from the medium to small particles there is a 20% reduction in radius and similarly moving from the medium to large there is a 20% increase in radius.

Identical simulations are then carried out in LAMMPS using the MDR contact model to provide a basis for comparison. To initialize the simulations, the spatial configuration of the particles is exactly recreated and the correct radii are assigned to each particle. Six rigid walls are defined to enclose the particles with the same kinematic control sequence specified. Two contact models are defined to mimic the normal and tangential interactions simulated in FEM. The normal interaction is governed by the MDR contact model with adhesion turned off. The input parameters to this model are the Young's modulus E, Poisson's ratio ν, yield stress Y, and critical confinement ratio ψ_b. To match FEM we define $E/Y = 20$ and $\nu = 0.3$. The critical confinement ratio ψ_b is set to 0.125 to match the simulation presented in Section 7. In the tangential direction a linear history (LH) dependent model is defined governed by Coulomb's law. This model has three inputs the tangential spring stiffness k_t, tangential friction coefficient μ_t, and a dimensionless multiplier $x_{\gamma,t}$ that determines the magnitude of the tangential damping. To mimic FEM, $\mu_t = 0.5$ and $x_{\gamma,t} = 0$ to avoid damping in the tangential direction. For consistency with the simulation presented in Section 7, the tangential stiffness k_t is selected to scale linearly with E and R_{mean}, where the latter is the mean particle radius for the simulation.

To appreciate the difference in computational expense between the two methods we note that MPFEM via Abaqus took 5.5 hours to complete in parallel using 10 processors on a 24-core machine @ 3.2 GHz and DEM via LAMMPS took approximately 1 second on the same machine in serial.

During compaction for both the FEM and DEM simulations the stresses in each of the principal directions σ_{xx}, σ_{yy}, and σ_{zz} are monitored. These stresses are calculated by summing the normal interaction forces on the walls and dividing by the available wall contact area, taking into consideration their movement. The resulting normalized stress-displacement curves are shown in Fig 6. Here, the macroscopic wall displacement Δ is normalized by W, which is the initial orthogonal distance from the box center to the rigid flats. The top row of Fig. 6 shows the results for the monodisperse simulation with panel (a), (b), and (c) corresponding to σ_{xx}, σ_{yy}, and σ_{zz}, respectively. Nice agreement is seen between the FEM and DEM results overall with only a slight over-prediction of the stress in the σ_{zz} direction at the highest displacements. Good agreement between the two simulation techniques is also seen for the tridisperse case shown in Fig. 6d-f. Overall, the MPFEM investigation demonstrates the robustness of the many-interacting particle scheme presented in Section 2.2 to reliably predict the behavior of many-interacting particles in both monodisperse and polydisperse situations.

5. Deformed particle reconstruction

The mechanically-derived nature of the MDR contact model allows insight into physical contact properties beyond the force-displacement relation including: contact area, contact pressure distribution, plastic surface displacements, and particle volume. This endows the MDR contact model with a unique capability to accurately capture an elastic-plastic particle's permanent shape change during loading.

5.1. *Triaxial compaction*

As an initial demonstration of this capability, we consider triaxial compaction loading by six rigid flats of a single homogeneous elastic-perfectly plastic particle with an initial radius R_o obeying a von Mises yield criterion as shown in Fig. 7a. The material parameters are the Young's modulus E, Poisson's ratio ν, and yield stress Y. The loading is kinematically driven with all rigid flats being displaced in-sync towards the particle center by a distance δ_o. To provide a ground truth for the deformation, a finite element simulation in Abaqus is run, with $E/Y = 20$, $\nu = 0.3$, and $\delta_o/R_o = 0.15$. The resulting deformed particle shape after removing the applied load is shown in Fig. 7a.

An identical triaxial compaction loading using the same material parameters and displacement is then carried out with the MDR contact model. At each of the six contacts the contact state variable δ_{max} is tracked, additionally the particle state variable R for the apparent radius is continuously updated by sourcing information from all active contacts. The tracking of these contact and particle state variables allows reconstruction of the deformed unloaded particle, as shown in Fig. 7b.

Visual comparison of Fig. 7a and b shows the good agreement between the FEM and MDR contact model predictions.

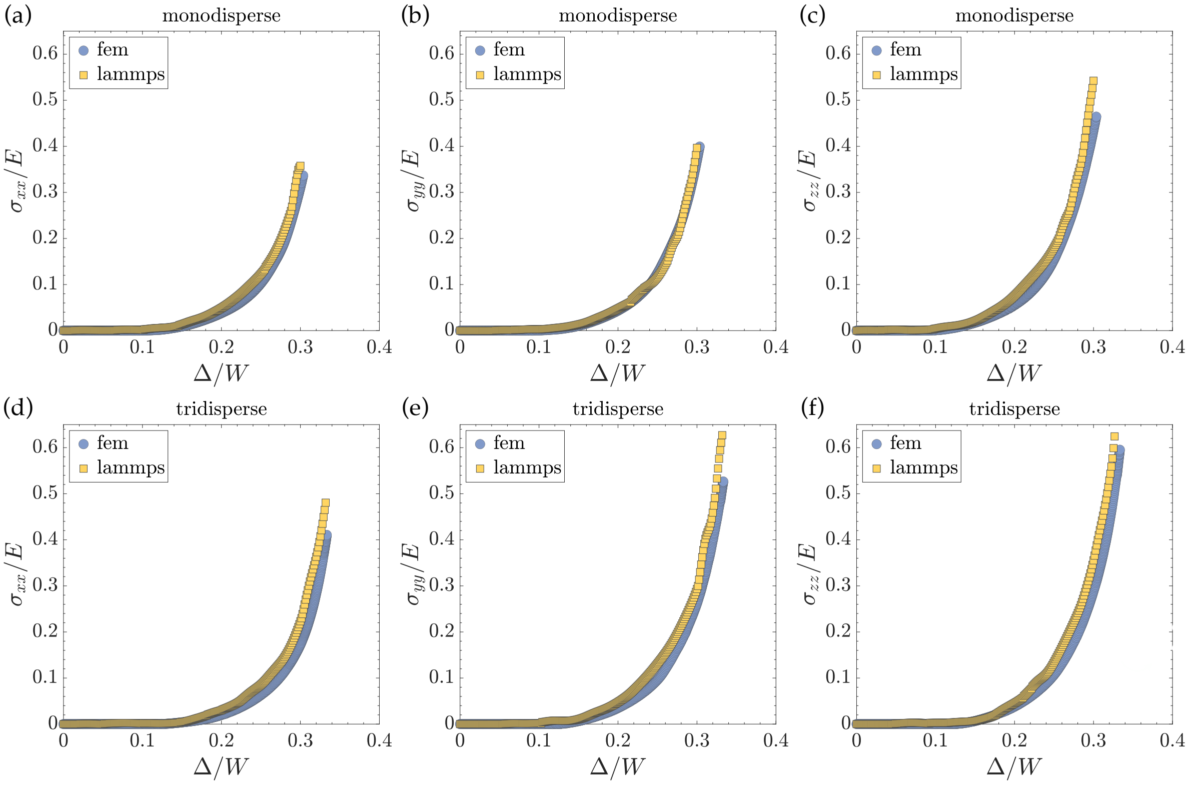

Figure 6: Normalized principal stress measurements on wall as a function of normalized wall displacement. Top row is monodisperse case: (a) σ_{xx}, (b) σ_{yy}, and (c) σ_{zz}. Bottom row is tridisperse case: (d) σ_{xx}, (e) σ_{yy}, and (f) σ_{zz}.

This unique ability of the MDR contact model to reconstruct the updated particle shape induced by plastic deformation aids in resolving a common deficit of elastic-plastic DEM whereby the deformation of a particle is not accessible. For a detailed quantitative comparison of the FEM and MDR contact model predictions in this loading case – including contact forces, contact areas, and elastic volume changes – please refer to [2].

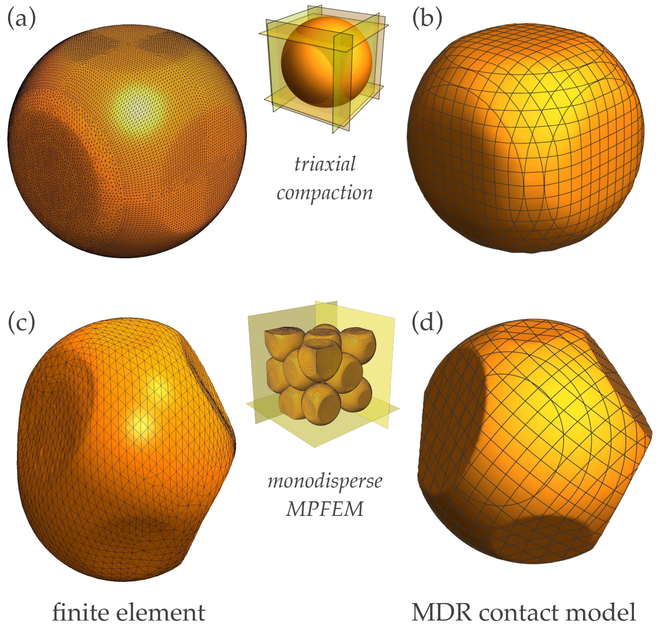

Figure 7: Deformed elastic-plastic particle shape after unloading for triaxial compaction predicted by the (a) FEM and (b) MDR contact model. Deformed elastic-plastic particle shape at maximum loading for the monodisperse MPFEM Particle 1 predicted by (c) FEM and (d) MDR contact model. Note that the lines on the MDR contact model reconstructions are for visualization purposes and do not represent a mesh.

5.2. *MPFEM*

The ability to reconstruct the deformed particle shape is not limited to simple loading configurations. To demonstrate the reconstruction for a more general loading, we examine the deformed shape of one of the fourteen particles involved in the monodisperse MPFEM simulation from Section 4 at the maximum compression as shown in Fig. 7c. We denote this particle of interest as Particle 1. The corresponding Particle 1 in the LAMMPS simulation is then also reconstructed based on the relevant state variables provided by the MDR contact model as shown in Fig. 7d.

To compare the kinematics of the two simulations, the displacement δ_o evolutions – measured with respect to and normalized by the initial radius R_o – for each active FEM contact on Particle 1 are compared to the corresponding MDR contact model predictions, as shown in Fig. 8. Two superscripts i and j are present on each of the displacements $\delta_o^{i,j}$. The first is always $i = 1$ to indicate Particle 1. The second $j \in [3, 4, 5, 6, 8, 9, 12, 13, 14]$ varies and indicates the other particle involved in the contact. For example, $\delta_o^{1,3}$ indicates the relative displacement between Particles 1 and 3. For reference, Appendix E contains more comparisons similar to Fig 7c and d so all active contacts may be viewed. On each plot of Fig. 8,

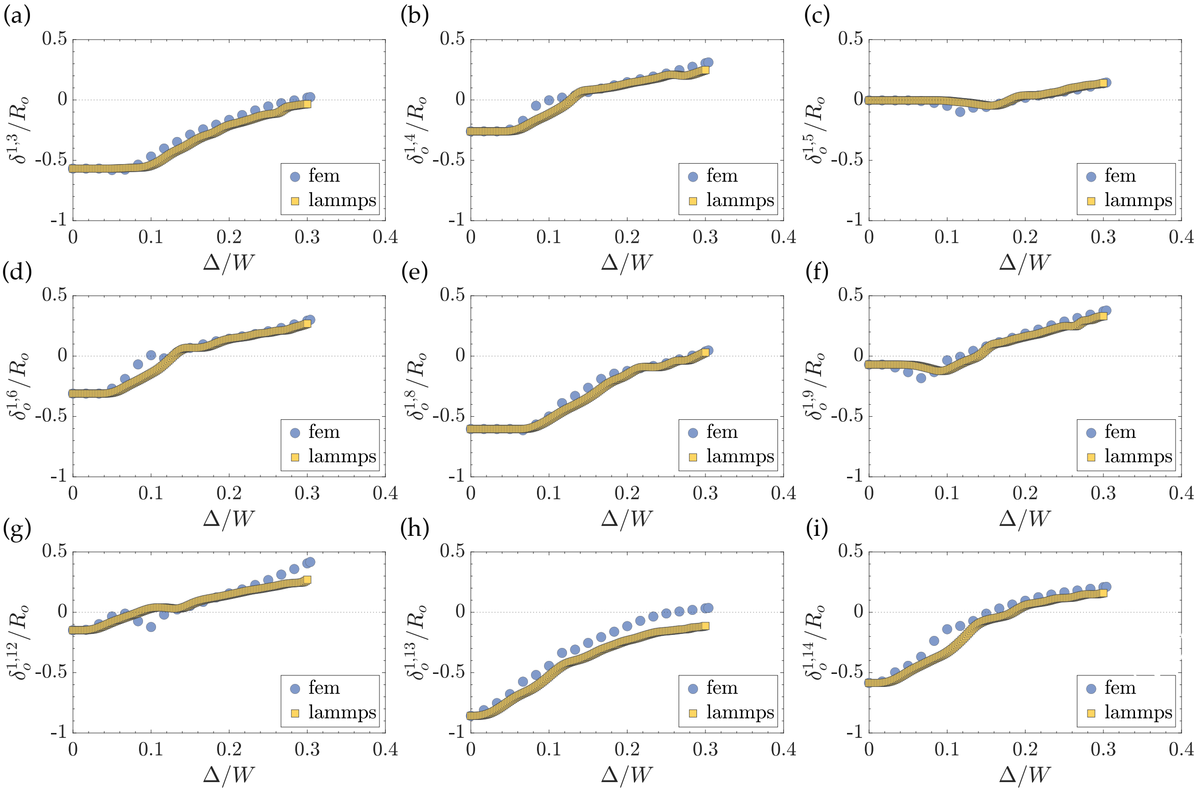

Figure 8: Particle 1's normalized displacement evolutions as a function of normalized wall displacement with Particle (a) 3, (b) 4, (c), 5, (d) 6, (e) 8, (f) 9, (g) 12, (h) 13, and (i) 14.

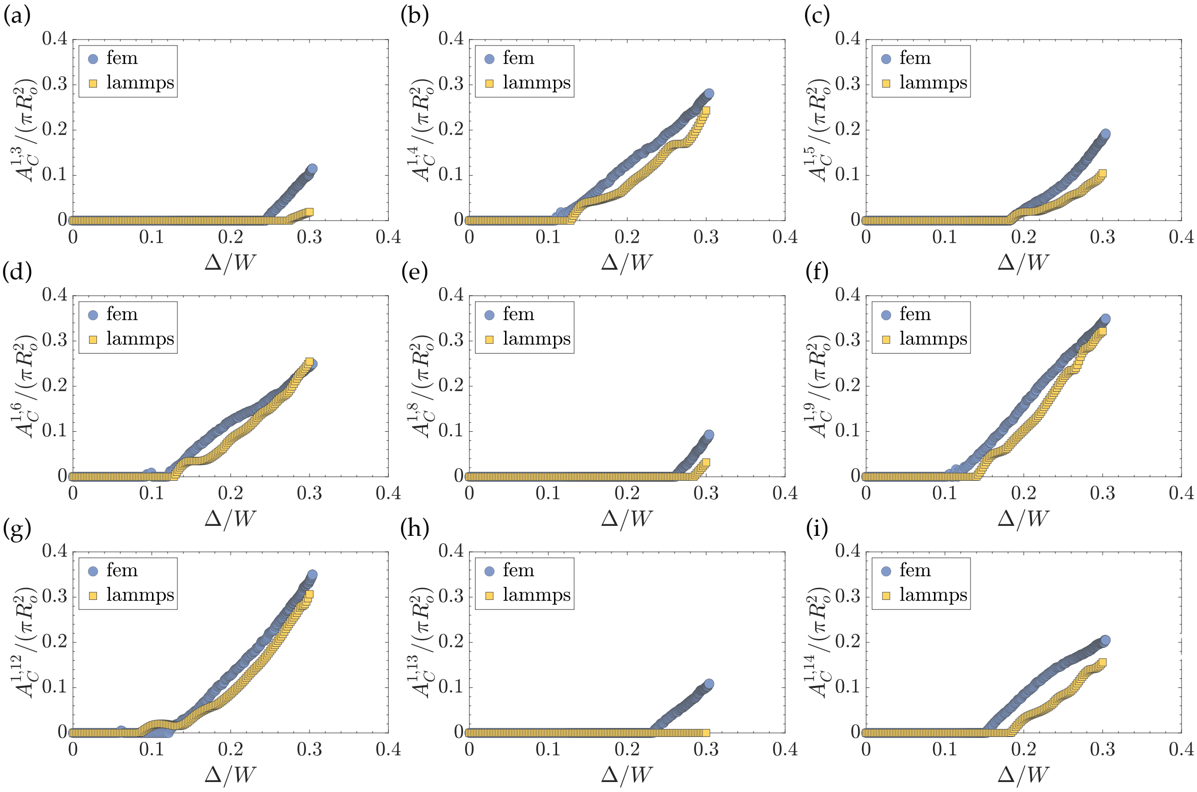

Figure 9: Particle 1's normalized contact area evolutions as a function of normalized wall displacement with Particle (a) 3, (b) 4, (c), 5, (d) 6, (e) 8, (f) 9, (g) 12, (h) 13, and (i) 14.

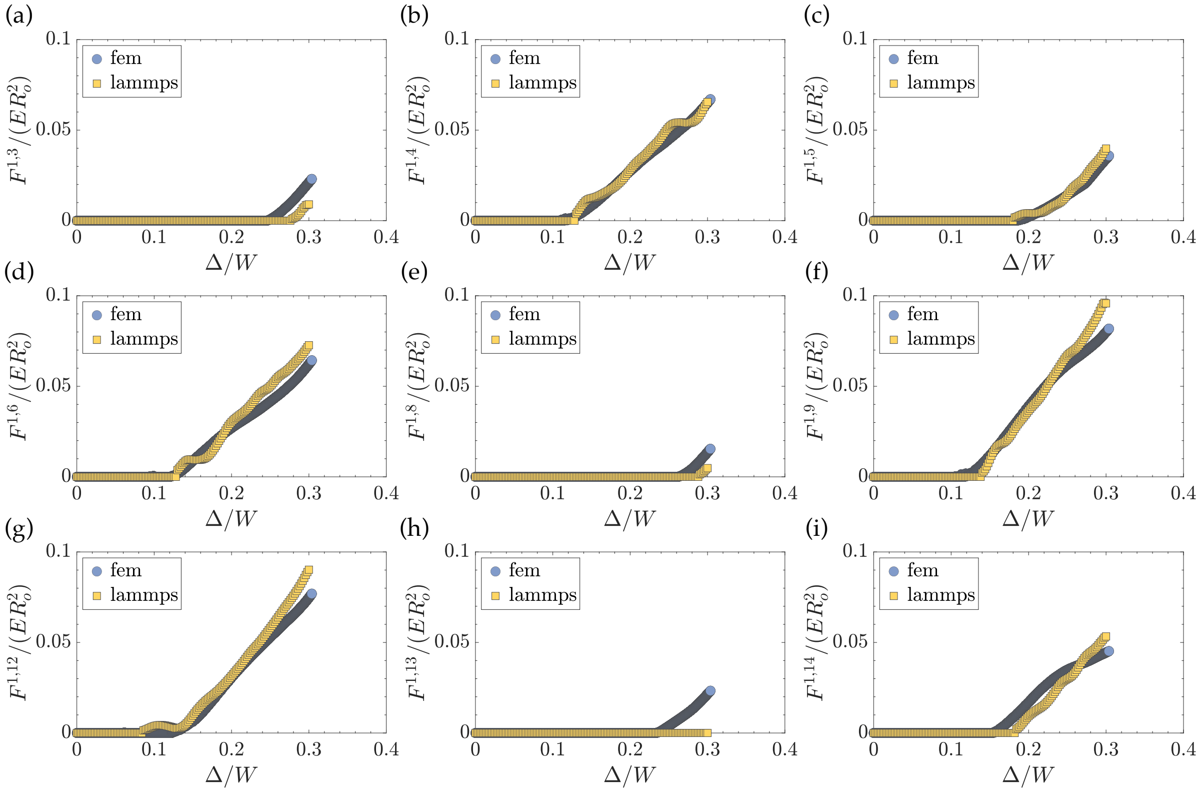

Figure 10: Particle 1's normalized force evolutions as a function of normalized wall displacement with Particle (a) 3, (b) 4, (c), 5, (d) 6, (e) 8, (f) 9, (g) 12, (h) 13, and (i) 14.

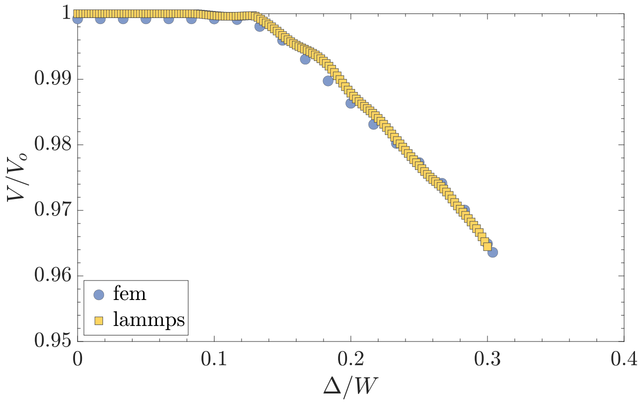

Figure 11: Normalized particle volume evolution as a function of normalized wall displacement.

a dotted line is drawn at zero displacement to help indicate the transition from non-contact to contact, which corresponds to negative and positive displacement, respectively. Overall, the displacement evolutions between the FEM and LAMMPS simulations match well indicating that the LAMMPS simulation properly reproduces the system's motion.

To measure the quality of the individual contact reconstructions, the contact area A_C evolution for each active FEM contact on Particle 1 is compared to the corresponding MDR contact model predictions as shown in Fig. 9. Each contact area is normalized by the cross sectional area πR_o^2. Nine total contacts exist on Particle 1 of the FEM simulation, however, it can be seen that the LAMMPS simulation does not detect contact $A_C^{1,13}$ shown in Fig. 9h. This is attributed to the inability of the MDR contact model, and classical DEM more generally, to capture anisotropic deformations induced by shear that tend to elongate particles along one axis, a point that is further discussed in Appendix E. Nevertheless, the remaining eight contact areas are all detected by the LAMMPS simulation and their evolutions are modeled to a reasonable degree of accuracy.

To complete the study of individual contact properties between the two simulations, the forces F at each contact are compared as shown in Fig. 10. Each force in this case is normalized by ER_o^2. Consistent with the fact that $A_C^{1,13}$ was zero throughout its evolution, $F^{1,13}$ shown in Fig 10h is also zero throughout. All remaining contacts, however, show a matching force evolution between the two simulations.

To quantify the accuracy of the deformed shape reconstruction provided by the MDR contact model at a particle level, a comparison of Particle 1's volume V evolution with FEM is presented in Fig. 11. In the plot, V is normalized by the initial particle volume V_o. The volume evolutions from the two simulations show good agreement.

The cumulative studies comparing individual contact displacements, areas, and forces, as well as particle volume evolution between the two simulation techniques, reveal the MDR contact model's robust ability to model individual particle deformations under complex non-symmetric loading conditions. Importantly, this modeling ability is achieved at a small fraction of the computational time, enabling larger systems to be modeled than would be feasible with the MPFEM alone[2].

6. Pharmaceutical tableting: experimental setup

The experimental set-up used to collect data is the compaction simulator[3] shown in Fig. 12. The cylindrical die, indicated by a darker gray color, has a diameter of 8 mm. The upper and lower cylindrical flat-faced punches both have a diameter of slightly less than 8 mm providing the following punch–die clearances: 40-50 μm for the upper and 25-30 μm for the lower. Both punches are instrumented with force sensors and two radial pressure sensors line the inside surface of the die. The experiments are conducted under displacement-controlled conditions at a loading rate of 1 mm/s and an unloading rate of 0.25 mm/s; these rates are chosen to be slow so as to minimizes any effects of air. Prior to testing, the die-walls are lubricated. The powder under consideration is Avicel PH102 (microcrystalline cellulose) as shown in Fig. 13, a commonly used pharmaceutical excipient that exhibits ductile behavior. The D50 particle diameter is 116 μm and the true material density ρ is 1560 kg/m^3. The tests are conducted to a specific relative density $RD = \rho_t/\rho$, where ρ_t is the bulk density of the tablet. In particular, two tests are carried out, one to a relative density of 0.85 and another to 0.99, corresponding to initial sample masses of 203.8 and 247.2 mg, respectively. Consistent with the methodology used in [31], post-processing local extrapolation of the axial and radial compaction curves was done to ensure stable parametrization.

The axial force sensors and radial pressure sensors allow the axial[4] and radial stress to be monitored, respectively, as a function of relative density. The measured upper punch axial stresses is shown in Fig. 14a. The compaction curves both start at a relative density of 0.34 and gradually increase in stiffness as the relative density rises. The peak forces are 96.5 MPa and 297.5 MPa for the tests corresponding to maximum relative densities of 0.85 and 0.99, respectively. For these tests, some elastic deformation is recovered, leading to nonlinear unloading curves that terminate at relative densities of 0.82 and 0.95, respectively.

Fig. 14b shows the measured radial stress evolution, where the displayed curve is an average of the upper and lower pressure sensor measurements. Akin to the axial stress measurement, a gradual stiffening is seen throughout compaction. For the test corresponding to a relative density of 0.85, the peak radial stress is 42.5 MPa, and the residual stress is 11.5 MPa. In contrast, for the test with a relative density of 0.99, the peak radial stress is 176 MPa, and the residual stress is 31 MPa.

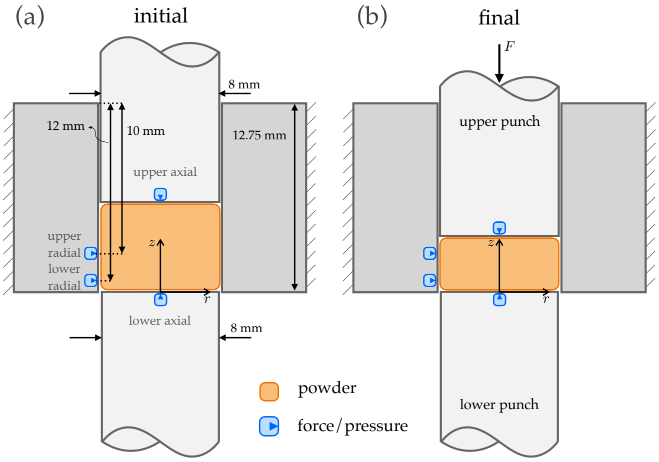

Figure 12: Compaction simulator instrumented with axial force sensors and radial pressure sensors. (a) Initial setup pre-compaction and (b) final configuration post-compaction.

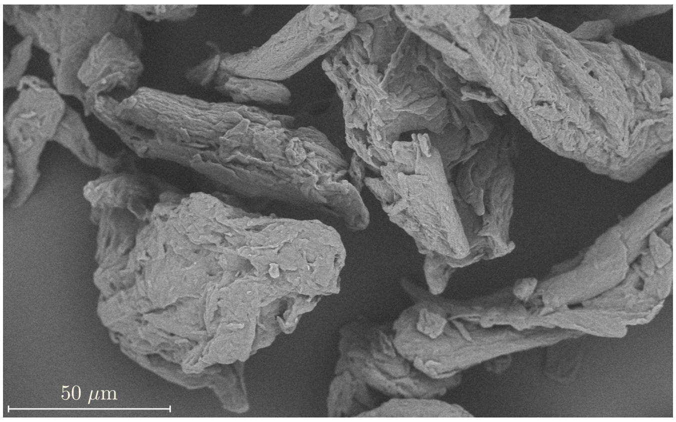

Figure 13: Scanning electron microscope (SEM) image of Avicel PH102 sample.

7. Pharmaceutical tableting: experimental and numerical comparison

7.1. Model and parameter selection

To enable comparison between the experimental compaction simulator results and a DEM simulation, the exact tablet press geometry including the upper punch, lower punch, and die is reconstructed in LAMMPS as shown in Fig. 14c. To create DEM particles representative of Avicel PH102, three types of contact models are defined: normal, tangential, and rolling.

The normal interaction is governed by the MDR contact model allowing for adhesive elastic-plastic contact. The input parameters to this model are the Young's modulus E, Poisson's ratio ν, yield stress Y, effective surface energy $\Delta\gamma$, and critical confinement ratio ψ_b. A simple damping model, governed by a viscosity η_n, is also defined in the normal direction.

In the tangential direction a linear history (LH) dependent model governed by Coulomb's law is defined. This model has three inputs the tangential spring stiffness k_t, tangential friction coefficient μ_t, and a dimensionless multiplier $x_{\gamma,t}$ that determines the magnitude of the tangential damping. Here, we

---

[2] In practice, the MDR contact model should be employed for predominately isotropic loading conditions, as studied here, given that plastic shear strains are only modeled adjacent to contacts and not deep within a particle's interior.

[3] The name compaction simulator becomes a misnomer in work involving numerical simulations. Compaction simulator describes a highly instrumented tableting press commonly used in the pharmaceutical industry to experimentally study and optimize the compaction of different powders.

[4] The axial stress is calculated from the axial force divided by the punch face surface area.

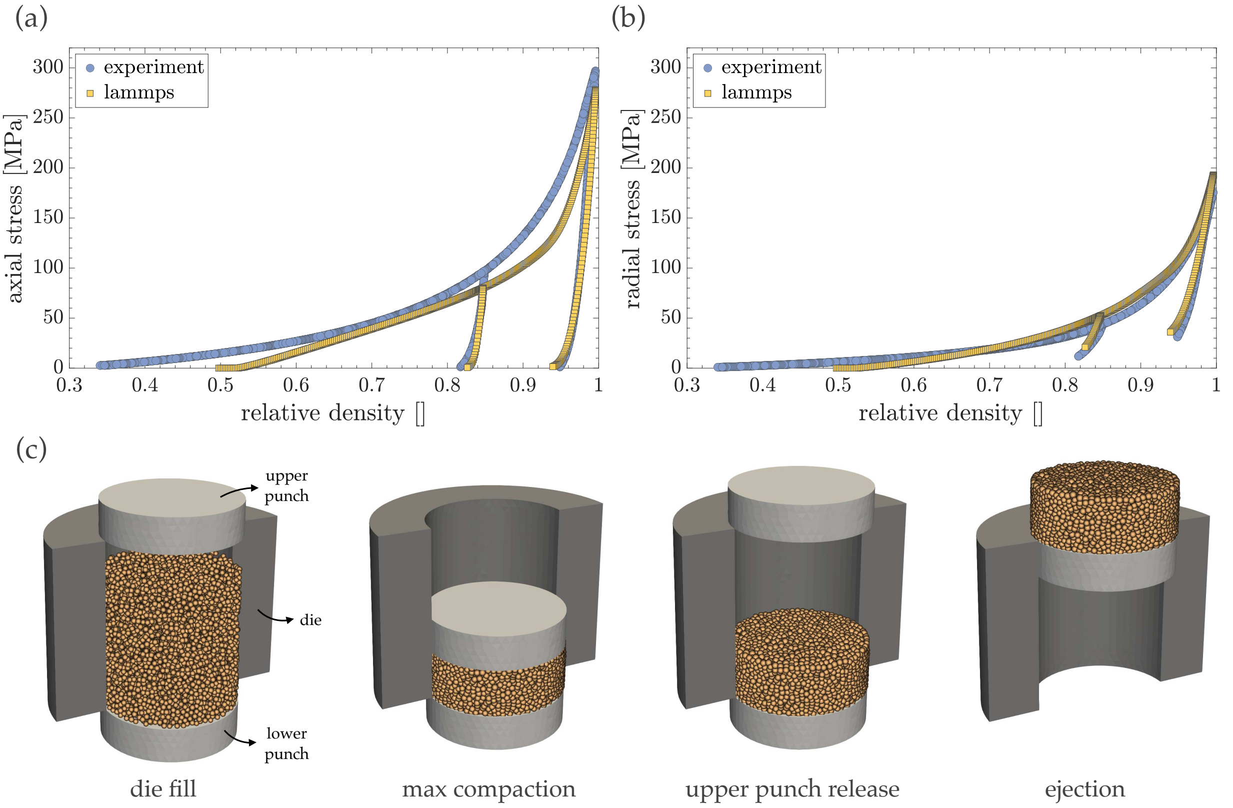

Figure 14: Experimental and simulation Avicel PH102 tableting results. (a) Axial stress-relative density plot and (b) radial stress-relative density plot. (c) Snapshots of LAMMPS compaction sequence involving material representative of Avicel PH102.

allow for two definitions of the tangential friction coefficient depending on the interaction type: particle-particle interactions μ_t and particle-wall $\mu_{t,\text{wall}}$.

The rolling resistance model is based on a spring–dashpot–slider (SDS) and takes three inputs including the rolling stiffness k_{roll}, rolling viscosity γ_{roll}, and a static rolling coefficient μ_{roll}. For details on the formulation of both the tangential and rolling resistance models see [56, 57].

A scaled version of Avicel PH102's true particle size distribution, provided by Vertex Pharmaceuticals, is used to sample particle radii from. The sampling is taken between an upper and lower radius bound denoted by R_{min} and R_{max}, respectively. For additional details regarding the particle size distribution see Appendix F. The true density ρ of all particles is constant and taken to match the manufacturers data sheet.

Table 1 details the numerical values used for the parameters in the LAMMPS simulation. For the normal contact model three of the values E, ν, and $\Delta\gamma$ are selected to fall within the range of reported literature values for Avicel PH102 [58, 59, 31]. The selection of $\Delta\gamma$ is roughly made indirectly via its relationship to the critical stress intensity factor $K_{Ic} = \sqrt{2\Delta\gamma E_c^*}$, where E_c^* is the composite plane strain modulus, due to K_{Ic} being more commonly measured and reported. Importantly, adhesion is applied only to particle-particle contacts, and although it is possible, no adhesion is simulated for particle-wall contacts. No reports in the literature on Avicel PH102 yield stress could be located, necessitating a fitting of Y, however, the selected value falls within the expected range for organic materials [60]. The value for ψ_b is tuned to trigger the high confinement bulk response stiffening in alignment with the experimental results. The η_n is set to scale with $\rho R_{\text{mean}}^2 v_p$, where v_p is the average velocity of the upper punch.

For tangential contact, k_t is selected to scale linearly with both E and R_{mean}. Damping in the tangential direction is set to match the normal damping by assigning $x_{\gamma,t} = 1.0$. The tangential friction coefficients μ_t and $\mu_{t,\text{wall}}$ are considered tunable parameters, and different values are defined for particle-particle and particle-wall contact. For particle-particle contact μ_t is selected to best match the experimental macroscopic stress evolutions in forward loading with particular focus on the dense high confinement regime. In the case of particle-wall contact, $\mu_{t,\text{wall}}$ is adjusted to approximately match the experimentally measured ejection force.

For the rolling model, k_{roll} also scales linearly with E and R_{mean}, with an additional squared dependence on μ_{roll}. To assign damping for the rolling direction, γ_{roll} is set to equal η_n[5]. The selection of μ_{roll} mostly influences the relative density just after die-filling and was set to 1.0 to obtain a very loose fill.

The time step Δt of the simulation is set by $0.08\sqrt{m/k}$, where $m = \rho 4/3\pi R_{\text{min}}^3$ is the mass of the smallest particle and $k = \kappa R_{\text{min}}$ is an effective stiffness related to the bulk elastic response.

---

[5] The fact that γ_{roll} shares dimensional units with η_n is due to the 'psuedo-force' formulation of the rolling resistance model.

The resulting time step based on the defined properties is $\Delta t = 1.1 \times 10^{-8}$ s. This formulation for the time step serves as a general guide to ensure numerical stability based on experience with the tableting simulation under consideration. However, it is subject to change depending on the compact geometry and loading conditions, which can change the effective stiffness due to the nonlinear nature of the contact model.

Normal (MDR)	**Tangential (LH)**
$E = 8\,\mathrm{GPa}$	$k_t = \frac{2}{7} E R_{\mathrm{mean}}$ N/m
$\nu = 0.3$	$x_{\gamma,t} = 1.0$
$Y = 77\,\mathrm{MPa}$	$\mu_t = 0.3$
$\Delta\gamma = 900\,\mathrm{J/m^2}$	$\mu_{t,\mathrm{wall}} = 0.1$
$\psi_b = 0.125$	
$\eta_n = 1e4 \rho R_{\mathrm{mean}}^2 v_p$ kg/s	
Rolling (SDS)	**Particle**
$k_{\mathrm{roll}} = \frac{9}{4} \mu_{\mathrm{roll}}^2 E R_{\mathrm{mean}}$ N/m	$R_{\mathrm{min}} = 139\,\mu\mathrm{m}$
$\gamma_{\mathrm{roll}} = \eta_n$	$R_{\mathrm{max}} = 160\,\mu\mathrm{m}$
$\mu_{\mathrm{roll}} = 1.0$	$\rho = 1560\,\mathrm{kg/m^3}$

Table 1: Values of parameters used in the LAMMPS simulation.

7.2. Simulation setup and results

The simulation is kinematically controlled and consists of four stages: die filling, compaction, release, and ejection as shown in Fig. 14c. During die filling, 10,000 particles are randomly sampled from the defined particle radius distribution of Appendix F. The sampled particles are then inserted in a spatially homogeneous, but random manner, one-by-one into the entire length of the empty die space between the upper and lower punch shown in the die fill panel of Fig. 14c. Upon insertion, each particle is assigned zero velocity and its position is checked to ensure it is initially non-overlapping with all other particles. Throughout the simulation no additional particles are added. At zero-time the particles are allowed to settle under the action of gravity, towards the lower punch, creating a loose packing. The packing then undergoes compaction whereby the top punch compresses the particles. The upper punch follows a sinusoidal displacement profile through time. The release continues the sinusoidal displacement until the upper punch returns to its original position. Ejection of the formed tablet occurs via movement of the lower punch upward; the upper punch moves upward as well during this time to provide clearance for the tablet. Specific compaction speeds and loading sequence timings are omitted because of the rate-independent nature of the defined contact models[6] Additionally, the inertia of the grains was measured to be sufficiently below an average contact force ensuring a quasi-static simulation.

To match the experimental setup, two simulations are carried out to relative densities of 0.85 and 0.99. The same initial packing is used in both simulations with only the upper punch strokes adjusted to achieve the desired relative density. Videos showcasing all phases of the tableting simulations for the two relative densities are shown in the Supplementary Video 1 and 2.

Throughout the simulations, the total force exerted on the upper punch by the particles is tracked. The resulting axial stress-relative density curves are shown in Fig. 14a. Due to the intraparticle porosity of Avicel PH102 there is discrepancy in the initial relative densities of the compaction curves between experiment and LAMMPS. This issue could be addressed with methods like pre-imposed particle clustering [61], but is out of the current scope of this paper given the focus on the dense high compaction regime. Beyond a relative density of around 0.6 to 0.8, good agreement between the experiment and LAMMPS is observed. After a relative density of 0.8 the LAMMPS simulation underpredicts the axial stress as the compact reaches high confinement and transitions to a response primarily dominated by bulk elasticity. However, this underprediction is anticipated for the MDR contact model based on the single particle die-compaction results of [2][7]. Nevertheless the LAMMPS prediction rejoins the experimental curve near the peak relative density and shows good agreement in both unloading cases. The good match during unloading indicates that the simulation is capturing the elastic spring-back of the tablet.

A per-particle stress at each step is also calculated during the simulations. Averaging this per-particle stress over all particles in the system and multiplying by the volume fraction gives the average stress tensor for the tablet. The radial stress is then computed by averaging the two normal stress components orthogonal to the axis of compaction. The resulting radial stress-relative density compaction curve is shown in Fig. 14b. Nice agreement between the experiments and LAMMPS simulations is seen in forward loading beyond a relative density of 0.6. During unloading we note that the simulations correctly predict a similar non-zero residual radial stresses to that of the experiment with the prediction for the relative density case of 0.99 being better than the 0.85 case.

To enhance the understanding of how different input parameters in the three defined contact models affect the overall compaction curves, a sensitivity analysis has been conducted and is presented in Appendix G.

The model's mechanically derived nature, combined with its ability to accurately reproduce macroscopic stress measurements for Avicel PH102, underscores its utility as a tool for analyzing the physics of powder compaction. In particular, it provides valuable insights into the microscopic origins of factors influencing key compact properties, such as residual stresses as discussed in Appendix G. By linking particle-level mechanical properties to critical macroscopic characteristics like residual stress, this approach can help practitioners optimize formulations and reduce related defects.

---

[6] Damping in the normal direction for the range of compaction speeds tested was shown to not alter the final results.

[7] The MDR contact model assumes a sharp transition to the bulk elastic response causing it to miss some of the gradual stiffening between the fully-plastic and bulk elastic regimes.

8. Conclusion

In this paper, we have focused on expanding the capabilities of large deformation adhesive elastic-plastic powder compaction modeling with DEM. This is achieved by extending the recently proposed MDR contact model – a mechanically-derived large deformation adhesive elastic perfectly-plastic contact model – to the many-interacting particle case. The method of extension is shown to be accurate even for cases of polydispersity enabling simulation of more realistic radii distributions.

Special contact considerations for large deformation DEM are discussed. It is shown that reliance on geometric overlap alone for contact force evaluation under large deformation conditions is flawed because non-physical contact through obstructing particles may occur. A new topological penalty algorithm for refined contact force evaluation is proposed and validated for a variety of test cases.

The extended MDR contact model and the topological penalty algorithm are implemented in the open-source DEM software LAMMPS for download and usage. The implementation is tested against MPFEM involving initially spherical meshed elastic perfectly-plastic particles. Two loadings are considered: a monodisperse case with fourteen particles and a tridisperse case with twelve particles. Macroscopic stress measurements show good agreement between the LAMMPS implementation and MPFEM.

Reconstruction of the deformed particle shapes using the MDR contact model and comparisons to FEM are presented for two different situations. Good qualitative agreement between the two is observed demonstrating the MDR contact models unique capability to accurately track deformations of individual particles. Quantitative comparisons of contact displacements, areas, and forces as well as the particle volume underscore the predictive accuracy of the MDR contact model.

To illustrate the practical applicability of the extended MDR contact model the problem of pharmaceutical tableting is considered. Experimental compaction simulator results for axial and radial stress as a function of relative density are presented for compaction of Avicel PH102 (microcrystalline cellulose). An identical tooling geometry is reconstructed with the LAMMPS implementation and the process of tablet compaction is simulated. The behavior of Avicel PH102 is represented by three defined contact models: the MDR contact model (normal), linear-history (tangential), and spring-dashpot-slider (rolling). Good predictive capability of the numerical simulation is shown through comparison of the axial and radial stress measurements. Notably, similar residual radial stress measurements are observed between experiment and simulation.

The extension of the MDR contact model to the many-interacting particle case and introduction of the topological penalty algorithm present strides towards significantly improved large deformation powder compaction simulations. Correlations between measurable macroscopic responses and fundamental particle material properties are more readily made due to the mechanically-derived nature of the MDR contact model, which relies primarily on measurable mechanical properties of the grains. Enhanced access to per-particle deformations and per-contact information such as contact areas and bond strength between adhered particles are also available. These features lay important groundwork to assist in unraveling the complex physics that govern powder compaction.

Looking ahead, this work opens several avenues for future research. Reformulating the many-interacting MDR contact model to accommodate varying material properties would enable the modeling of multi-component formulations. Further parametric studies, beyond those conducted in Appendix G, using the provided implementation could help elucidate how microscopic material parameters influence residual stresses post-powder compaction and their relationship to tablet defects. Additionally, fluid-coupled simulations with DEM, incorporating the extended MDR contact model and a compressible gas phase, could be performed. These simulations may offer insights into the role of entrapped air in defect formation, shedding light on their microscopic origins in pharmaceutical tableting. The many-interacting MDR contact model could also aid in developing constitutive relations for cohesive powders [62, 63, 64]. Beyond pharmaceutical tableting, the proposed implementation could be applied to processes like calendaring in battery manufacturing [65, 66, 67], with the aim of enhancing battery performance.

Declaration of competing interest

The authors declare that they have no known competing financial interests or personal relationships that could have appeared to influence the work reported in this paper.

Acknowledgments

The authors acknowledge the support of the National Science Foundation Graduate Research Fellowship Program (NSF-GRFP) and the International Fine Particle Research Institute (IFPRI) (Grant ARR-109-01). The authors would like to thank Dan Bolintineanu and Joel Clemmer from Sandia National Laboratories for their help with implementing the extended MDR contact model into LAMMPS.

Appendix A. Review of MDR contact model formulation

It is noted that the structure of this summary heavily relies on the descriptions given in the original publications [1, 2].

The full MDR contact model with a bulk elastic response, or simply the MDR contact model for short, is guided by the superposition of elastic states whereby the boundary tractions are attributable to two sources: (i) a MDR portion and (ii) a bulk uniform compaction. This leads naturally to the resulting contact force F being composed of a MDR and bulk contribution

$$\boxed{F = F_{\text{MDR}} + F_{\text{Bulk}}}. \tag{A.1}$$

In laying out the formulation of the MDR contact model we first cover the kinematics in Appendix A.1. Next, the MDR force contribution and adhesive formulation are detailed in Appendix A.2 and Appendix A.3, respectively. The formulation is then completed with the description of the bulk elastic force contribution in Appendix A.4. For reference all model parameters are tabulated in Table A.2.

Appendix A.1. Kinematics

Similar to the contact force, there is a natural kinematic decomposition of the displacement δ_o into a MDR and bulk component

$$\delta_o = \delta_{o,\text{MDR}} + \delta_{o,\text{Bulk}}. \tag{A.2}$$

The quantity δ_o captures the overlap with respect to the initial particle radius R_o. Within the MDR contact model framework, an additional radius exists, known as the apparent radius R. Its value is larger than or equal to R_o, and accounts for a particle's free surface displacement attributable to the incompressibility of plastic deformation. Prescription for how R is calculated is given in Appendix A.2. Associated with the apparent radius, is the apparent overlap δ which measures overlaps with respect to R. The relationship between δ and δ_o is

$$\delta = \delta_o + R - R_o. \tag{A.3}$$

Evolution of $\delta_{o,\text{MDR}}$ and $\delta_{o,\text{Bulk}}$ is carried out by partitioning incremental changes in the displacement $d\delta_o$ based on the confinement ratio $A_{\text{free}}/A_{\text{tot}}$

$$\begin{aligned} d\delta_{o,\text{MDR}} &= d\delta_o, & d\delta_{o,\text{Bulk}} &= 0 & &\text{if } \frac{A_{\text{free}}}{A_{\text{tot}}} \geq \psi_b, \\ d\delta_{o,\text{MDR}} &= d\delta_o - d\bar{\delta}_o, & d\delta_{o,\text{Bulk}} &= d\bar{\delta}_o & &\text{otherwise,} \end{aligned} \tag{A.4}$$

where A_{free} is a particle's free surface area not part of any contact, A_{tot} the total particle surface area, and $d\bar{\delta}_o$ is the mean surface displacement across all contacts. As seen in (A.4), the triggering of the bulk response is governed by the critical confinement ratio ψ_b, a user determined value that specifies the $A_{\text{free}}/A_{\text{tot}}$ value corresponding to the bulk elastic regime. This criterion is a direct measurement of the remaining pore space around a particle, with $A_{\text{free}}/A_{\text{tot}} = 0$ corresponding to complete closure of pore space (i.e., total confinement). For a more detailed description of ψ_b, discussion on other methods for determining the onset of the bulk elastic regime, and graphical depictions of single contact force-displacement responses that include the bulk elastic regime, please see [2].

To determine A_{free} and A_{tot} the total area involved in contact on a given particle A_{con} is calculated by simply summing the contact areas A_C of all active contacts N

$$A_{\text{con}} = \sum_{i=1}^{N} A_{C,i}, \tag{A.5}$$

where

$$A_{C,i} = \pi(2\delta_i R - \delta_i^2) + c_{A,i}. \tag{A.6}$$

The subscript i denotes individual contacts in these expressions and is omitted when defining the parameters. In (A.6), c_A is the contact area intercept defined in Appendix A.2.

With (A.5) established, the total particle area is given as

$$A_{\text{tot}} = 4\pi R^2 - 2\pi \sum_{i=1}^{N} (\delta_{\text{max,MDR,i}} + \delta_{o,\text{Bulk,i}}) R + A_{\text{con}}, \tag{A.7}$$

where $\delta_{\text{max,MDR}}$ is the maximum experienced MDR apparent overlap also defined in Appendix A.2. The free area not involved in contact is then given as

$$A_{\text{free}} = A_{\text{tot}} - A_{\text{con}}. \tag{A.8}$$

Finally, $d\bar{\delta}_o$ is calculated by determining the mean surface displacement increment across all contacts

$$d\bar{\delta}_o = \frac{1}{A_{\text{con}}} \sum_{i=1}^{N} (A_{C,i} \boldsymbol{n}_i \cdot d\boldsymbol{\delta}_{o,i}). \tag{A.9}$$

In the above equation, $\boldsymbol{n}$ is the contact normal and $d\boldsymbol{\delta}_o$ is the contacts vector-valued incremental displacement.

Appendix A.2. MDR force contribution

The MDR force is given as a function of the MDR apparent overlap δ_{MDR}, maximum experienced MDR apparent overlap $\delta_{\text{MDR,max}}$, and apparent radius R

$$\begin{aligned} F_{\text{MDR}}(\delta_{\text{MDR}}, \delta_{\text{MDR,max}}, R) = \frac{E_c^* AB}{4} \Bigg[& \arccos\left(1 - \frac{2\delta_{\text{1D}}^e}{A}\right) \\ & - \left(1 - \frac{2\delta_{\text{1D}}^e}{A}\right) \sqrt{\frac{4\delta_{\text{1D}}^e}{A} - \frac{4(\delta_{\text{1D}}^e)^2}{A^2}} \Bigg]. \end{aligned} \tag{A.10}$$

Prior to the onset of plasticity, $\delta_{\text{1D}}^e = \delta_{\text{MDR}}$ in the elastic regime. Since contact is always considered to be between a deformable particle and rigid flat, the composite plane strain modulus reduces to

$$E_c^* = \frac{E}{1 - \nu^2}. \tag{A.11}$$

where E is the particle's Young's modulus and ν its Poisson's ratio. The MDR apparent overlap and maximum experienced MDR apparent overlap are 'displacements' measured with respect to the apparent radius R, and thus have similar forms to that of (A.3)

$$\begin{aligned} \delta_{\text{MDR}} &= \delta_{o,\text{MDR}} + R - R_o, \\ \delta_{\text{MDR,max}} &= \delta_{o,\text{MDR,max}} + R - R_o. \end{aligned} \tag{A.12}$$

where $\delta_{o,\text{MDR,max}}$ is the maximum experienced MDR displacement. The transformed representation of the contacting body is taken to be elliptical and parameterized by A and B which have different forms for the elastic and plastic regime

$$\begin{aligned} A &= 4R, & B &= 2R, & &\text{elastic} \\ A &= \frac{4p_Y}{E_c^*} a_{\text{max}}, & B &= 2a_{\text{max}}, & &\text{fully-plastic.} \end{aligned} \tag{A.13}$$

The contact average pressure in the fully-plastic regime p_Y is taken to be equivalent to the average pressure of a contact involving a rigid-plastic sphere and rigid flat

$$p_Y = Y\left(1.75\exp\left(-4.4\delta_{\mathrm{MDR,max}}/R\right) + 1\right). \tag{A.14}$$

A sharp transition occurs between the elastic and fully-plastic regimes and is based on the average contact pressure. Specifically, once the average pressure defined by Hertz's contact law

$$\bar{p}_H = \frac{4E_c^*}{3\pi\sqrt{R}}\sqrt{\delta}, \tag{A.15}$$

intersects the hardening curve (A.14) the formulation switches from elastic to fully-plastic. The transformed 1D elastic displacement has the form

$$\delta_{\mathrm{1D}}^e = \frac{\delta_{\mathrm{MDR}} - \delta_{\mathrm{MDR,max}} + \delta_{\mathrm{1D,max}}^e + \delta_R}{1 + \delta_R/\delta_{\mathrm{1D,max}}^e}, \tag{A.16}$$

where

$$\delta_{\mathrm{1D,max}}^e = A/2. \tag{A.17}$$

The displacement correction used to extend the half-space approximation to admit large deformation is given as

$$\begin{aligned}\delta_R =& \frac{F(\delta_{\mathrm{MDR,max}}, \delta_{\mathrm{MDR,max}}, R)}{\pi a_{\mathrm{max}}^2} \\ &\times \left[\frac{2a_{\mathrm{max}}^2(\nu - 1) - z_R(2\nu - 1)(\sqrt{a_{\mathrm{max}}^2 + z_R^2} - z_R)}{2G\sqrt{a_{\mathrm{max}}^2 + z_R^2}}\right],\end{aligned} \tag{A.18}$$

where the free the distance from the sphere center to free surface is

$$z_R = R - (\delta_{\mathrm{MDR,max}} - \delta_{\mathrm{1D,max}}^e). \tag{A.19}$$

The maximum experienced contact radius is given by

$$a_{\mathrm{max}} = \sqrt{(2\delta_{\mathrm{MDR,max}}R - \delta_{\mathrm{MDR,max}}^2) + c_A/\pi}, \tag{A.20}$$

where c_A is solved for to ensure a continuous contact radius between the elastic and plastic regimes

$$c_A = \pi(\delta_Y^2 - \delta_Y R). \tag{A.21}$$

By equating $\bar{p}_H$ and p_Y the yield displacement δ_Y may be solved for

$$\frac{4E_c^*}{3\pi\sqrt{R}}\sqrt{\delta_Y} = Y\left(1.75\exp\left(-1.1\delta_Y/R\right) + 1\right). \tag{A.22}$$

The apparent radius is allowed to grow, provided the bulk elastic response is not on, to respect the incompressible nature of the plastic deformation. This leads to the incremental form

$$\Delta R = \begin{cases}\max\left[\frac{\Delta V^e - \sum_{i=1}^N \pi\Delta\delta_{o,\mathrm{MDR},i}(2\delta_{o,\mathrm{MDR},i}R_o - \delta_{o,\mathrm{MDR},i}^2 + R^2 - R_o^2)}{2\pi R\sum_{i=1}^N(\delta_{o,\mathrm{MDR},i} + R - R_o) - 4\pi R^2},\ 0\right], & \text{if } \frac{A_{\mathrm{free}}}{A_{\mathrm{tot}}} \geq \psi_b, \\ 0, & \text{otherwise.}\end{cases} \tag{A.23}$$

The elastic volume change ΔV^e (positive for compressive increments) arises from the difference in volume between steps, with the total volume V evaluated as

$$V = V_o\left(1 + \frac{1}{3\kappa V}\mathrm{tr}\left(\sum_{c\,\in\,V} \boldsymbol{f}^c \otimes \boldsymbol{b}^c\right)\right), \tag{A.24}$$

where V_o is the initial volume and κ is the bulk modulus. The quantities $\boldsymbol{f}$ and $\boldsymbol{b}$ represent the force and branch vectors respectively.

Appendix A.3. MDR adhesion

Incorporating JKR-type fracture mechanics-based adhesion into the MDR framework is a straightforward process. The central concept involves allowing the springs to adhere to the indenter surface. During decompression, these springs stretch under tension until reaching a critical extension length Δl that is related to the contact radius a and effective surface energy $\Delta\gamma$

$$\Delta l(a) = \sqrt{\frac{2\pi a\Delta\gamma}{E_c^*}}, \tag{A.25}$$

To simplify the adhesion formulation we assume that material may only adhere once compressed[8]. During unloading, springs detach and the current contact radius needs to be continually compared to the the critical contact radius a_c which is given by

$$\left.\frac{dg_{\mathrm{1D}}(a)}{da}\right|_{a=a_c} = \xi\sqrt{\frac{\pi\Delta\gamma}{2E_c^* a_c}}, \qquad \xi = \begin{cases}3, & \text{force-control,} \\ 1, & \text{displacement-control,}\end{cases} \tag{A.26}$$

to determine whether full separation should occur. For the assumed elliptical indenter the 1D gap function takes on the form

$$g_{\mathrm{1D}}(a) = \frac{A}{2} - \frac{A}{B}\sqrt{\frac{B^2}{4} - a^2}. \tag{A.27}$$

While unloading the normal surface displacement at the edge of the contact must be tracked

$$w_{\mathrm{1D}}(a) = \delta_{\mathrm{1D}}^e - g_{\mathrm{1D}}(a), \tag{A.28}$$

and compared to $\Delta l(a)$. Three possible adhesive states at the contact are possible based on this comparison:

1. **No tensile springs:** $w_{\mathrm{1D}}(a) = 0$
   In this case, no springs are in a tensile state and the adhesive force is zero. The force formulation from Appendix A.2 holds without modification.
2. **Tensile springs, but not exceeding critical length:** $0 < w_{\mathrm{1D}}(a) \leq \Delta l(a)$
   In this case, part of the contact is in tension, but no springs exceed the critical length, so detachment does not occur. The total force can be determined by superposing

---

[8] Based on experimental observations, the JKR theory of adhesion predicts that when two bodies are brought sufficiently close together, they will spontaneously form a finite contact area without any applied external load. We neglect this effect.

two problems: non-adhesive contact and adhesive retraction. The non-adhesive force contribution $F_{\text{n.a.}}$ is treated directly setting $\delta = g_{\text{1D}}(a)$ in (A.10). The adhesive retraction involves uniformly decompressing the springs by $\delta^e_{1D} - g_{\text{1D}}(a)$ leading to

$$F_{\text{a.r.}} = 2E^*_c(\delta^e_{1D} - g_{\text{1D}}(a))a. \tag{A.29}$$

The total force is the sum of the non-adhesive and adhesive retraction contributions

$$F_{\text{MDR}} = F_{\text{n.a.}} + F_{\text{a.r.}} \tag{A.30}$$

3. **Tensile springs exceed critical length:** $w_{\text{1D}}(a) > \Delta l(a)$ In this case, the outer springs have stretched beyond the critical length, requiring detachment. To determine whether a new stable equilibrium exists or if full separation occurs, we must find the contact radius that satisfies

   $$\delta^e_{\text{1D}} + \Delta l(a) - g_{\text{1D}}(a) = 0. \tag{A.31}$$

   If this contact radius is greater than the critical radius $a > a_c$ the contact remains intact, and the process from Case 2 is applied to find the total force using the updated radius. If the new radius is less than the critical radius $a < a_c$ the contact fully separates.

Adhesion at a contact is allowed to redevelop after separation if the surfaces contact are loaded in compression again. Note that adhesion only alters the MDR portion of the force and is calculated purely from the MDR kinematic quantities.

Appendix A.4. Bulk elastic force contribution

The bulk force contribution at a given contact i is most easily written in incremental form

$$dF_{\text{Bulk},i} = \frac{A_{\text{con}}}{V_{\text{geo}}}\kappa\, d\bar{\delta}_o\, A_{C,i}. \tag{A.32}$$

where V_{geo} is the deformed particle volume given by a purely geometric picture. Specifically, V_{geo} is expressed as

$$V_{\text{geo}} = \frac{4}{3}\pi R^3 - \sum_{i=1}^{N}\left(\frac{\pi}{3}\delta_i^2[3R - \delta_i]\right). \tag{A.33}$$

Integration of (A.32) then provides the full bulk force

$$F_{\text{Bulk},i} = \int dF_{\text{Bulk},i}, \qquad \delta_{o,\text{Bulk},i} = \int d\bar{\delta}_o. \tag{A.34}$$

It is important to note that the integrands are non-zero only after the system enters the bulk elastic state, where $A_{\text{free}}/A_{\text{tot}} < \psi_b$. Before this transition, all increments in bulk displacement remain zero, as determined by the upper case of (A.4).

A	height of elliptical indenter
A_{con}	area involved in contacts
A_{free}	free particle area
A_{tot}	total particle surface area
A_C	contact area
a	contact radius
a_c	critical contact radius
$a_{\max}$	maximum experienced contact radius
B	width of elliptical indenter
$\boldsymbol{b}$	branch vector
c_A	contact area intercept
δ_o	displacement
$\boldsymbol{\delta}_o$	displacement vector
$\bar{\delta}_o$	mean surface displacement
$\delta_{o,\text{MDR}}$	MDR displacement
$\delta_{o,\text{Bulk}}$	Bulk displacement
$\delta_{o,\max}$	maximum experienced displacement
δ	apparent overlap
δ_{MDR}	MDR apparent overlap
$\delta_{\max,\text{MDR}}$	MDR maximum experienced apparent overlap
δ^e_{1D}	transformed elastic displacement
$\delta^e_{\text{1D},\max}$	maximum transformed elastic displacement
δ_R	displacement correction
δ_Y	yield displacement
E	Young's modulus
E^*_c	composite plane strain modulus
F	contact force
F_{MDR}	force from MDR
F_{Bulk}	force from bulk elastic response
$F_{\text{n.a.}}$	non-adhesive force
$F_{\text{a.r.}}$	adhesive retraction force
$\boldsymbol{f}$	force vector
G	shear modulus
g_{1D}	1D gap function
$\Delta\gamma$	effective surface energy
κ	bulk modulus
Δl	critical extensional length
$\boldsymbol{n}$	contact normal
ν	Poisson ratio
$\bar{p}_H$	average pressure for Hertz contact
p_Y	average pressure along hardening curve
ψ_b	critical confinement ratio
R_o	initial radius
R	apparent radius
ΔR	change in apparent radius
V_o	initial volume
V	current volume
V_{geo}	deformed geometric particle volume
ΔV^e	change in elastic volume
w_{1D}	1D normal surface displacement
Y	yield stress
z_R	depth of particle center

Table A.2: MDR contact model with a bulk elastic response parameters.

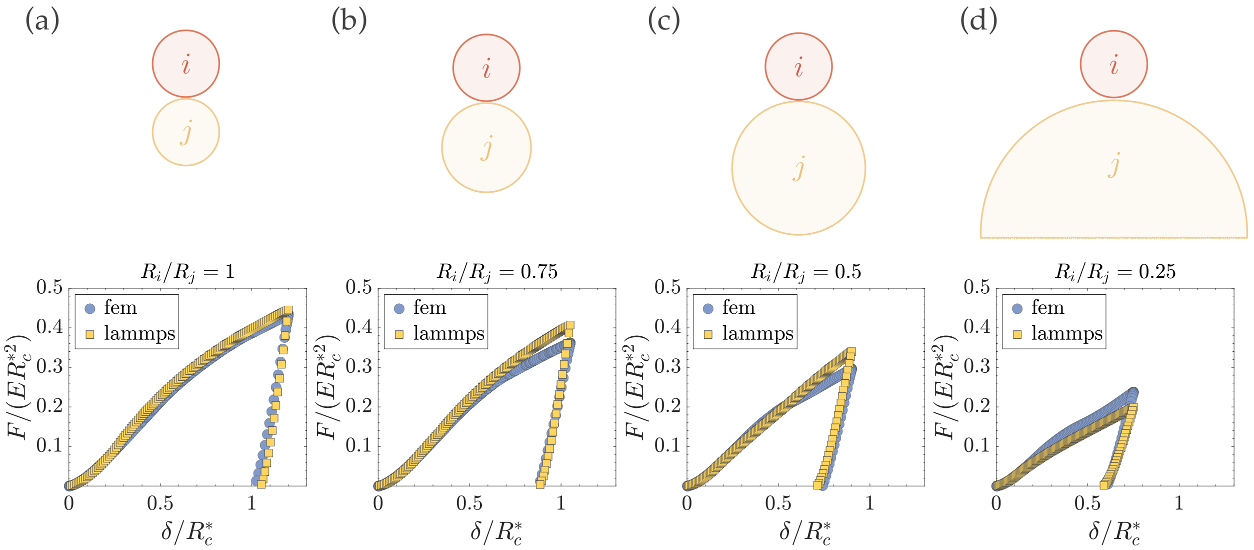

Figure A.15: FEM and LAMMPS comparison of resulting normalized force-displacement curves for particle-particle contact with varying radii. The radii ratios $R_i/R_j = [1, 0.75, 0.5, 0.25]$ correspond in order to (a), (b), (c), and (d).

Appendix B. Rigid flat placement scheme adjustment under extreme overlaps

In cases of significant compaction and polydisperity the overlaps δ/R experienced at a contact can approach 1. To avoid the non-physical placement of a rigid flat at $\delta/R \geq 1$ during forward loading (i.e., $\delta = \delta^{\max}_{\mathrm{geo}}$) a cap is placed on the allowable maximum experienced geometric apparent overlaps $\delta^{\max}_{\mathrm{i,geo}}$ and $\delta^{\max}_{\mathrm{j,geo}}$ of a contacting pair. This ensures that if the cap is reached, any additional displacement is partitioned to the contact side experiencing less overlap. In particular, there are two cases to consider

$$\begin{aligned} &\text{if } \delta^{\max}_{\mathrm{i,geo}}/R_i > 0.95: \quad \begin{cases} \delta^{\max}_{\mathrm{i,geo}} = 0.95R_i, \\ \delta^{\max}_{\mathrm{j,geo}} = \delta_{\max} - 0.95R_i, \end{cases} \\ &\text{if } \delta^{\max}_{\mathrm{j,geo}}/R_j > 0.95: \quad \begin{cases} \delta^{\max}_{\mathrm{i,geo}} = \delta_{\max} - 0.95R_j, \\ \delta^{\max}_{\mathrm{j,geo}} = 0.95R_j. \end{cases} \end{aligned} \tag{B.1}$$

The non-unique overlap limit of 0.95 is used for all simulations in this work.

Appendix C. Validation of rigid flat placement scheme for contacting particles of varying radii

To investigate the quality of force prediction between particles of varying radii provided by the rigid flat placement scheme, a series of FEM simulations are carried out. The simulations consist of contact between two elastic-perfectly plastic particles obeying a von Mises yield criterion with $E/Y = 20$ and $\nu = 0.3$. The material behavior is considered to be homogeneous and isotropic in both particles allowing for a 2D axisymmetric analysis of two hemispheres. Contact is kinematically controlled through tie constraints that impose displacements along the axis of symmetry. No displacement control is imposed in the radial direction on the flat faces of the hemispheres to allow radial expansion as it would naturally occur. The contact between the particles is modeled as rigid in the normal direction and frictionless in the tangential direction. The mesh is composed of CAX8R (8-node biquadratic axisymmetric quadrilateral, reduced integration) elements whose density was determined through a mesh refinement study.

The variation in radii studied in the FEM simulation is shown in Fig. A.15a-d. The top particle i has a fixed radius R_i throughout all simulations whereas the bottom particle j has a varying radius R_j. The relative radii ratios R_i/R_j simulated spans the following set $[1, 0.75, 0.5, 0.25]$. To normalize the plots the composite radius $R_c^* = (1/R_i + 1/R_j)^{-1}$ is used.

Identical simulations are replicated in LAMMPS for the same radii ratios. The resulting normalized force-displacement plots for both FEM and LAMMPS are shown in Fig. A.15a-d. Relatively good agreement is seen across the four cases in forward loading with the $R_i/R_j = 0.25$ case having the largest difference. The disagreement can be attributed to two factors that are apparent at larger deformations: (i) as the radii ratio grows the geometric intersection becomes a less accurate representation of the correct contact area during forward plastic loading and (ii) the larger the difference in radii the more disparity there is in the amount of plastic deformation accumulated, implying that the smaller particle can become fully yielded while the large particle is still relatively unyielded throughout. Despite the slight disagreement in forward loading for the smaller radii ratios, all of the LAMMPS unloading curves show good agreement with FEM, unloading to zero force at approximately the same δ/R_i.

These comparisons demonstrate the proposed rigid flat placements ability to predict the force between contacting particle of varying radii, a critical step in enabling reliable simulation of greater polydispersity.

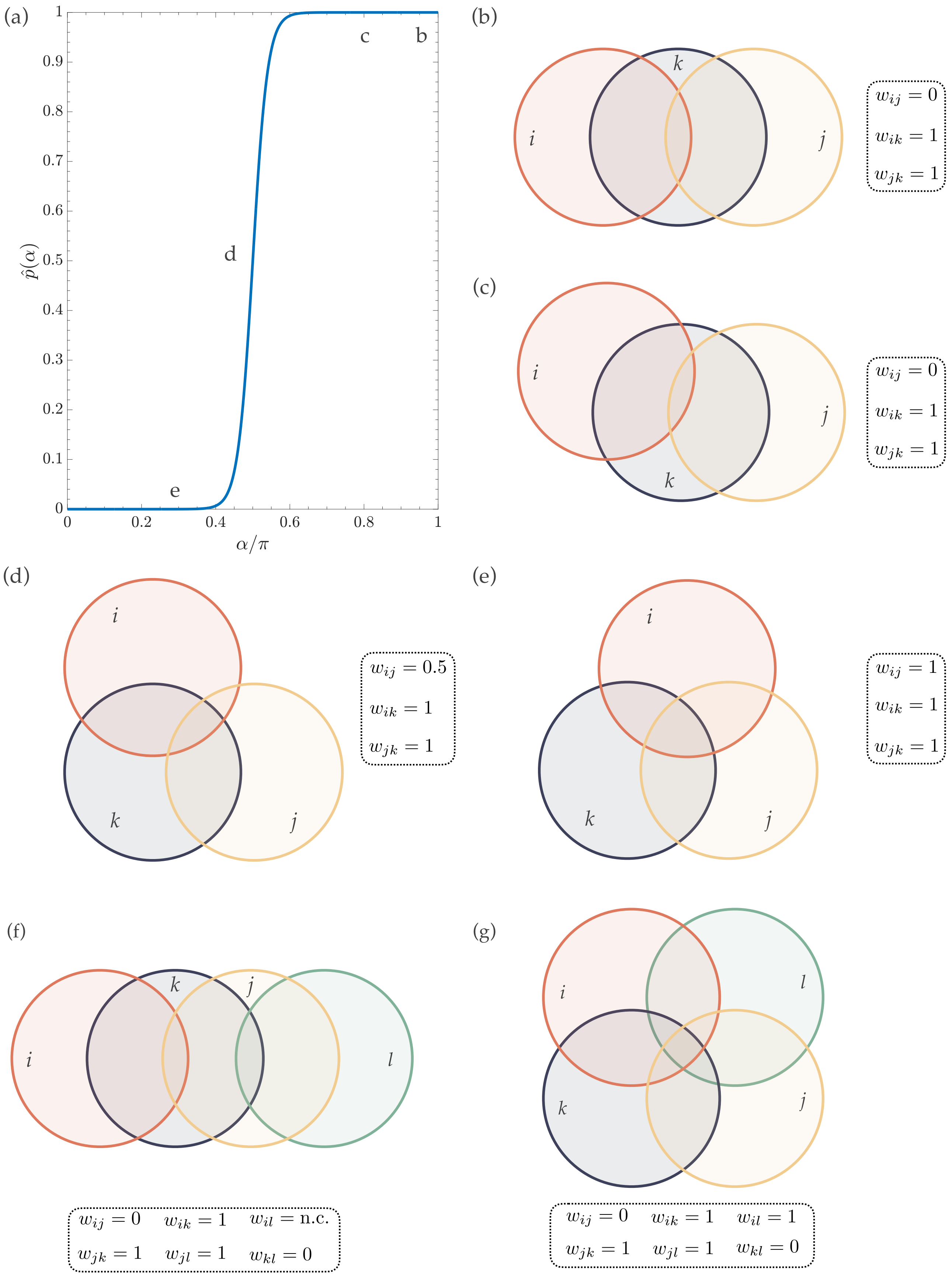

Figure C.16: Topological penalty algorithm examples. (a) Sigmoid penalty function. (b)-(e) Three particle contacts with associated penalties marked on plot (a) and weights. (f)-(g) Four particle contacts and associated weights.

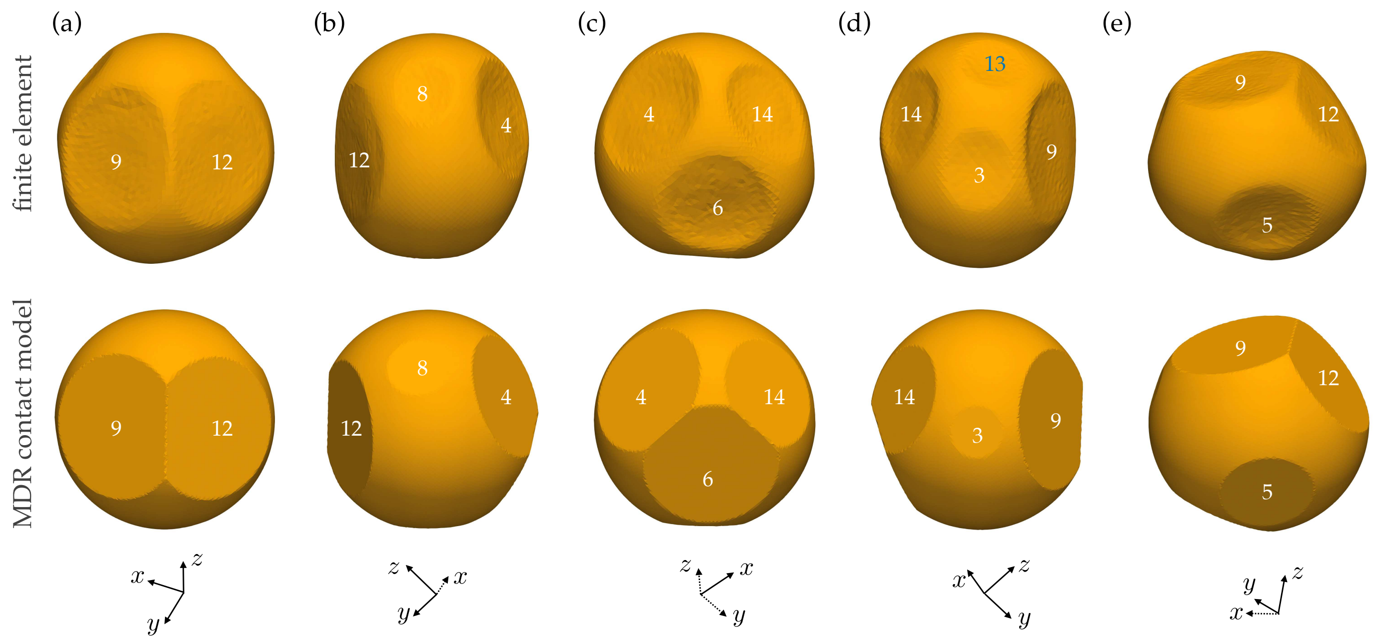

Figure C.17: Five different viewing angles (a)-(e) showing all active contacts on Particle 1 for both the finite element method and MDR contact model. Contact with Particle 13, shown in (d), is missed by the MDR contact model.

Appendix D. Topological penalty algorithm examples

The topological penalty algorithm presented in Section 3 is designed to identify non-physical contacts that occur through obstructing particles. To further understand the algorithm we present a plot of the sigmoid penalty function (9) used to determine contact weights in Fig. C.16a. The angle range over which the penalty changes from effectively[9] 0 to a value of 1 is approximately $0.4 \leq \alpha/\pi \leq 0.6$. This transition region is controlled by t_p the penalty transition intensity. For the plot shown in Fig. C.16a, and all simulations in this work, a value of $t_p = 50$ was used which gives physically reasonable results, however no unique value of t_p exists. Four distinct example triplet configurations of overlapping particles i, j, and k and their corresponding weights for each contact are depicted in Fig. C.16b-e. In each of the four arrangements the central particle is k meaning the only potential non-zero penalty will be p_{ij}. Its value for each case b-e is indicated along the sigmoid penalty function by the corresponding letter.

Fig. C.16b and c are cases where particle k fully obstructs contact of $\{i,j\}$. The topological penalty algorithm correctly identifies this and calculates $p_{ij} = 1$, $w_{ij} = 0$, and a subsequent zero force at contact $\{i,j\}$. In Fig. C.16d, contact $\{i,j\}$ is only partially obstructed. This is reflected in $p_{ij} = 0.5$, $w_{ij} = 0.5$, and a final force at contact $\{i,j\}$ that is half the calculated value. In the last triplet Fig. C.16e, no contact is truly obstructing the other leading to $p_{ij} = 0$, $w_{ij} = 1$, and a fully-weighted final force at contact $\{i,j\}$. This sequence of configurations shows the ability of the sigmoid penalty function to smoothly transition the weights and forces at each contact, avoiding any jumps, as particle i experiences a predominately shearing-like motion from Fig. C.16b to e. Importantly this smoothness is carried over even in the case of the central particle changing for a given triplet.

To further solidify the machinery of the topological penalty algorithm, we consider two cases of four overlapping particles i, j, k, and l as shown in Fig. C.16f and g. In this situation, there are now six potential contacts and four triplets. Considering first Fig. C.16f, we see that it is similar to Fig. C.16b with the addition of particle l at the far right. As anticipated, the scheme will correctly predict $p_{ij} = 1$ and $w_{ij} = 0$. Triplet $\{j, k, l\}$, will also be considered with j as the central particle totally obstructing contact $\{k, l\}$, meaning that $p_{kl} = 1$ and $w_{kl} = 0$. In this situation, the other triplets $\{i, k, l\}$ and $\{i, j, l\}$ do not meet the criterion that all three particles overlap each other therefore no penalties are assigned to the rest of the active contacts $\{i, k\}$, $\{j, k\}$, and $\{j, l\}$, leading full weights of one. Contact $\{i, l\}$ is labeled as not contacting (n.c.) meaning no penalty is even assigned.

Fig. C.16g is similar to Fig. C.16d with the addition of particle l in the upper right. In this case, each particle is central in one of the four triplets. This results in the diagonal contacts $\{i, j\}$ and $\{k, l\}$ being the non-central contact in two separate triplets meaning they are penalized twice. For example, contact $\{i, j\}$ is the non-central contact for the triplets $\{i, j, k\}$ and $\{i, j, l\}$. In both cases a penalty of 0.5 is calculated meaning $p_{ij} = p_{ij}^{ijk} + p_{ij}^{ijl} = 0.5 + 0.5 = 1$, where the superscript indicates the triplet associated with the penalty contribution. Conversion into a weight leads to $w_{ij} = 0$. The penalty and weight calculation process is identical for contact $\{k, l\}$, however it involves triplets $\{j, k, l\}$ and $\{i, k, l\}$. All other active contacts $\{i, k\}$, $\{j, k\}$, $\{i, l\}$, and $\{j, l\}$ are not penalized leading full weights of one.

---

[9] Effectively in this case is defined as the range $\hat{p}(\alpha) \in [0.01, 0.99]$

Appendix E. Further study of deformed particle reconstruction: Particle 1

Appendix E.1. Contact to particle mapping

To provide further visual analysis of Particle 1, five additional viewing angles displaying both the FEM and MDR contact model predictions are shown in Fig. C.17a-e. Each visible contact is provided a numbered label corresponding to the other particle involved in that contact. For example, in Fig. C.17a contacts with Particle 9 and 12 are shown. Inspection of all five viewing angles reveals that contact sizes and relative positions are nicely captured by the MDR contact model with the exception of Particle 13 as shown in Fig. C.17d.

Appendix E.2. Anisotropic deformations

As observed in Fig. C.17d, contact between Particle 1 and 13 is missed by the MDR contact model. This is attributable to the MDR contact model, and classical DEM more generally, being unable to capture anisotropic internal deformations. To illustrate this point, Fig. E.18a shows overlaid deformed reconstructions of Particle 1 and 13, where the MDR contact model is shown as a solid body and the FEM as a wireframe. As anticipated, the MDR contact model reconstructions do not overlap, whereas the FEM particles do. To quantify the degree of anisotropic deformation in each particle, minimum volume ellipses that fully encloses the deformed particles are fitted to each reconstruction [68], as shown in Fig. E.18b. For both of the MDR contact model reconstructions, the minimum volume ellipse reduces to essentially a sphere, indicating no anisotropy. On the other hand, the minimum volume ellipses fitted to the FEM reconstructions display anisotropy, as indicated by the variance in the semiaxes' lengths tabulated in Table E.3. The combined effect of both Particle 1 and 13's anisotropic deformation results in contact between the two particles not captured by the MDR contact model.

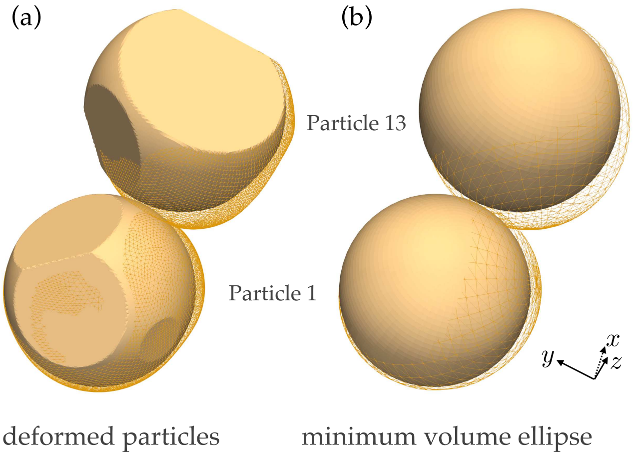

Figure E.18: Visual investigation of Particle 1 and 13 interaction. (a) Overlaid deformed particles predicted by the MDR contact model (solid) and FEM (wireframe). (b) Minimum volume ellipse fittings of each particle for the MDR contact model (solid) and FEM (wireframe) predictions.

Particle ID	**Semiaxes lengths**	**Principal axes**
	$(r_1; r_2; r_3)$	(n_x, n_y, n_z)
Particle 1	0.4751	(-0.3164, 0.5777, 0.7524)
	0.5184	(-0.9242, -0.3664, -0.1074)
	0.5577	(0.2136, -0.7294, 0.6499)
Particle 13	0.5083	(-0.3153, -0.0356, 0.9483)
	0.5504	(0.5269, -0.8377, 0.1437)
	0.5889	(0.7893, 0.5450, 0.2829)

Table E.3: Semiaxes lengths and principal axes directions of the minimum volume ellipses fitted to the deformed FEM Particles 1 and 13.

Appendix F. Avicel PH102 particle size distribution

The experimentally measured particle size distribution for Avicel PH102 is represented as a volume distribution and probability density function in Fig. F.19a and b, respectively.

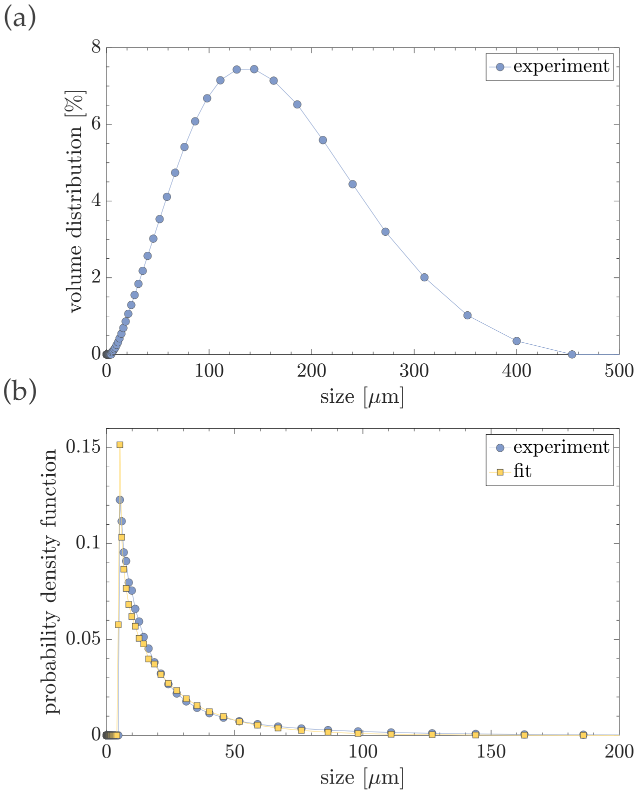

Figure F.19: Avicel PH102 particle size distribution represented as a (a) volume distribution and (b) probability density function.

A shifted Weibull distribution is used to provide a fit for the probability density function. The scale parameter $\lambda = 6$, the shape parameter $k = 0.69$, and the shift $s = 4.5$ leading to

$$\mathrm{PDF}_{\mathrm{Avicel}}(\mathrm{size}; \lambda, k, s) = \begin{cases} \frac{k}{\lambda}\left(\frac{\mathrm{size}}{\lambda}\right)^{k-1} e^{-\left(\frac{x}{\lambda}\right)^k}, & \mathrm{size} \geq s \\ 0, & \mathrm{size} < s \end{cases} \tag{F.1}$$

For computational tractability, a scaled up subset of (F.1) was sampled from to select the particle radii for the simulations of Section 7. In particular, the probability density function used in

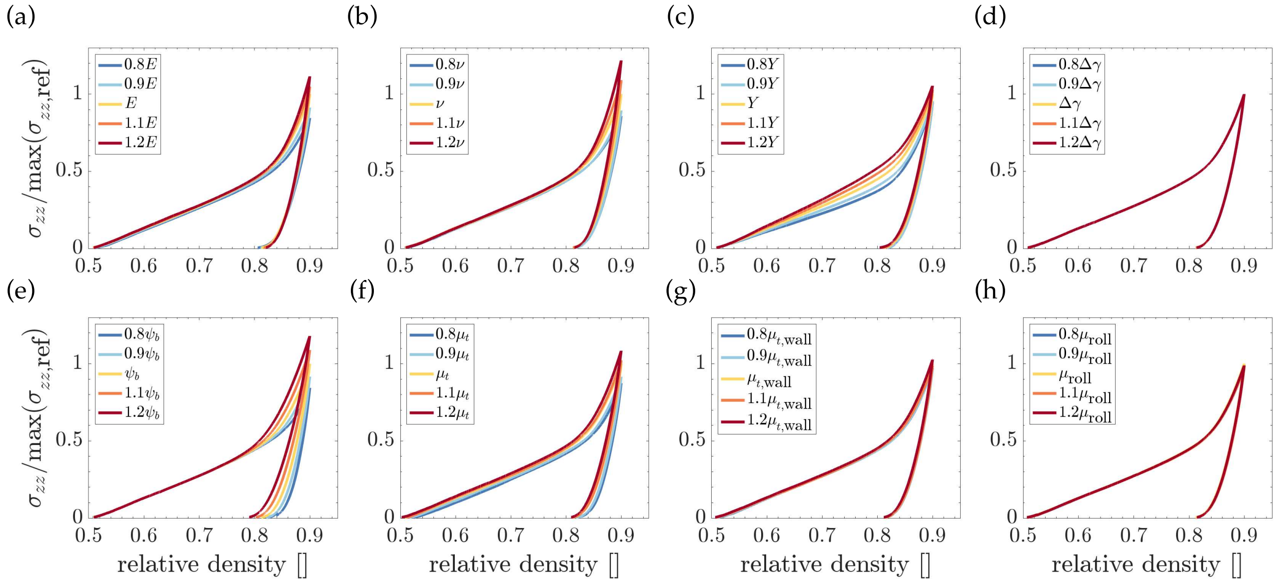

Figure F.20: Axial stress sensitivity to changes in input parameters: (a) E, (b) ν, (c) Y, (d) $\Delta\gamma$, (e) ψ_b, (f) μ_t, (g) $\mu_{t,\mathrm{wall}}$, and (h) μ_{roll}.

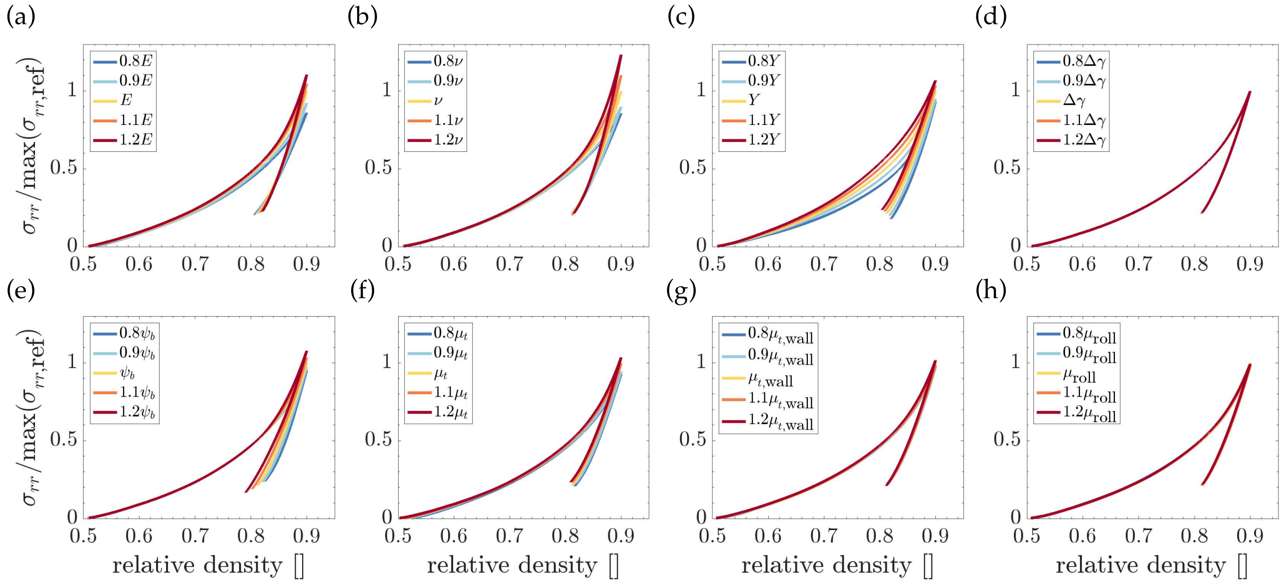

Figure F.21: Radial stress sensitivity to changes in input parameters: (a) E, (b) ν, (c) Y, (d) $\Delta\gamma$, (e) ψ_b, (f) μ_t, (g) $\mu_{t,\mathrm{wall}}$, and (h) μ_{roll}.

the LAMMPS tableting simulation is identical to (F.1) scaled by a factor of 3.2

$$\mathrm{PDF}_{\mathrm{lammps}} = \begin{cases} 3.2\frac{k}{\lambda}\left(\frac{\mathrm{size}}{\lambda}\right)^{k-1} e^{-\left(\frac{x}{\lambda}\right)^k}, & \mathrm{size} \geq 3.2s \\ 0, & \mathrm{size} < 3.2s \end{cases} \tag{F.2}$$

where only sampled particle radii between R_{min} and R_{max} were accepted for the simulation.

Appendix G. Input parameter sensitivity analysis

The resulting stress-relative density compaction curves are influenced by the input parameters of the three defined contact models: normal, tangential, and rolling. To examine the effect of each parameter on the compaction curves, a sensitivity analysis is conducted on a selected subset of parameters. For the normal MDR contact model, variations in E, ν, Y, $\Delta\gamma$, and ψ_b are analyzed. In the tangential model, the parameters μ_t and $\mu_{t,\mathrm{wall}}$ are studied, while for the rolling model, only μ_{roll} is considered.

To establish a baseline for comparison, a reference set of material parameters $\{E, \nu, Y, \Delta\gamma, \mu_t, \mu_{t,\mathrm{wall}}, \mu_{\mathrm{roll}}\}$ is selected. For each parameter, four variations from the reference are considered by either increasing or decreasing its value in increments of 10%. For example, for E, the four variations are $\{0.8E, 0.9E, 1.1E, 1.2E\}$. Each set of parameters, including the

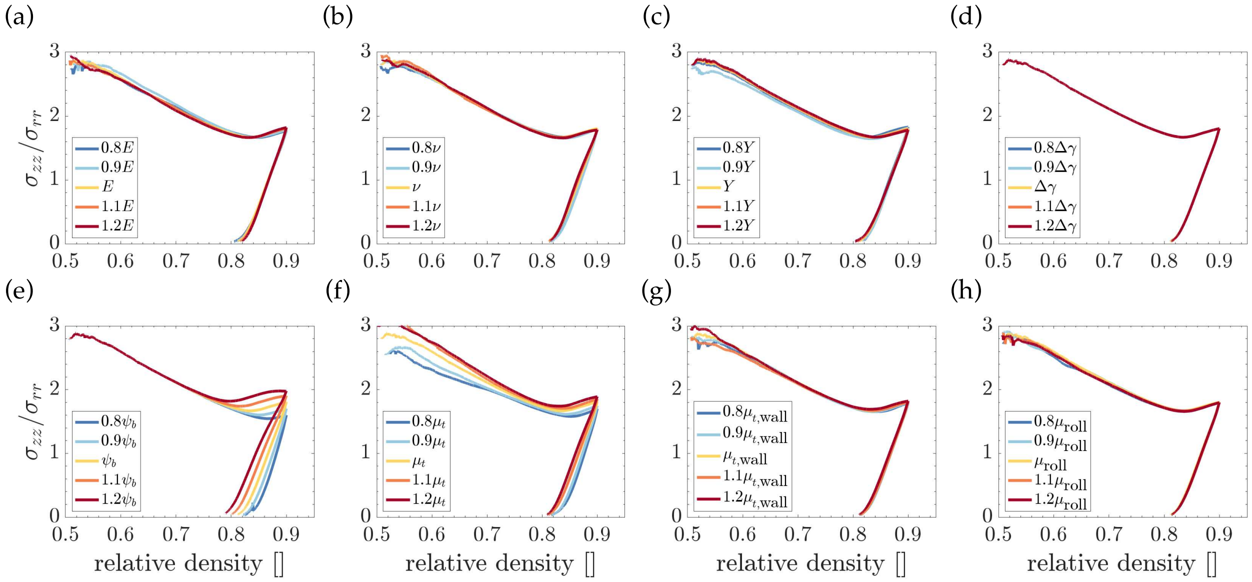

Figure F.22: Axial to radial stress ratio sensitivity to changes in input parameters: (a) E, (b) ν, (c) Y, (d) $\Delta\gamma$, (e) ψ_b, (f) μ_t, (g) $\mu_{t,\text{wall}}$, and (h) μ_{roll}.

reference, are compacted to a relative density of 0.9. The particle packing is the same for every test and consists of 1,000 polydisperse particles with $R_{\max}/R_{\min} = 1.15$. The resulting compaction curves for each parameter change are shown in Fig. F.20 and F.21, which display the axial stress-relative density and radial stress-relative density curves, respectively. The ratio between the axial and radial stress is shown in Fig. F.22. The general trends captured in these figures provides valuable reference points for calibration of the contact model parameters.

The results of the sensitivity analysis provide initial insight into how variations in each parameter affect the residual stress. For example, as E increases, ν decreases, or Y decreases, the residual stress tends to increase. Although $\Delta\gamma$ does not influence the overall compaction curve, decreasing its value lowers the residual stress. If reduced sufficiently, the tablet will fracture, causing the residual stress to drop to nearly zero. The critical confinement ratio ψ_b has a significant impact on residual stress, as it determines when radial growth of the particles, due to plasticity, ceases. As ψ_b increases, radial growth is halted earlier, leading to less buildup of radial stress and, consequently, a lower residual radial stress after unloading. Within the studied range of μ_t, the residual stress generally decreases as μ_t increases. Lastly, $\mu_{t,\text{wall}}$ and μ_{wall} have minimal influence on the residual stress.

References

[1] W. Zunker, K. Kamrin, A mechanically-derived contact model for adhesive elastic-perfectly plastic particles, part i: Utilizing the method of dimensionality reduction, Journal of the Mechanics and Physics of Solids 183 (2024) 105492.

[2] W. Zunker, K. Kamrin, A mechanically-derived contact model for adhesive elastic-perfectly plastic particles, part ii: Contact under high compaction—modeling a bulk elastic response, Journal of the Mechanics and Physics of Solids 183 (2024) 105493.

[3] W. B. James, High performance ferrous pm materials for automotive applications, Metal Powder Report 46 (9) (1991) 26–32.

[4] K. Ramesh, R. Sagar, Fabrication of metal matrix composite automotive parts, The International Journal of Advanced Manufacturing Technology 15 (1999) 114–118.

[5] J. Barrett, Powder metallurgy in aerospace applications, JOM 15 (1963) 349–351.

[6] V. A. R. Henriques, P. P. d. Campos, C. A. A. Cairo, J. C. Bressiani, Production of titanium alloys for advanced aerospace systems by powder metallurgy, Materials Research 8 (2005) 443–446.

[7] W. M. Sigmund, N. S. Bell, L. Bergström, Novel powder-processing methods for advanced ceramics, Journal of the American Ceramic Society 83 (7) (2000) 1557–1574.

[8] M. Çelik, Pharmaceutical powder compaction technology, CRC Press, 2016.

[9] Z. Li, L. Zhao, X. Lin, L. Shen, Y. Feng, Direct compaction: An update of materials, trouble-shooting, and application, International Journal of Pharmaceutics 529 (1-2) (2017) 543–556.

[10] S. C. Thakur, H. Ahmadian, J. Sun, J. Y. Ooi, An experimental and numerical study of packing, compression, and caking behaviour of detergent powders, Particuology 12 (2014) 2–12.

[11] C. Meyer, H. Bockholt, W. Haselrieder, A. Kwade, Characterization of the calendering process for compaction of electrodes for lithium-ion batteries, Journal of Materials Processing Technology 249 (2017) 172–178.

[12] M. Abdollahifar, H. Cavers, S. Scheffler, A. Diener, M. Lippke, A. Kwade, Insights into influencing electrode calendering on the battery performance, Advanced Energy Materials 13 (40) (2023) 2300973.

[13] A. Laptev, O. Vyal, M. Bram, H. Buchkremer, D. Stöver, Green strength of powder compacts provided for production of highly porous titanium parts, Powder Metallurgy 48 (4) (2005) 358–364.

[14] N. Shinohara, M. Okumiya, T. Hotta, K. Nakahira, M. Naito, K. Uematsu, Formation mechanisms of processing defects and their relevance to the strength in alumina ceramics made by powder compaction process, Journal of materials science 34 (1999) 4271–4277.

[15] M. Anuar, B. Briscoe, Detrimental consequences of the paracetamol tablet elastic relaxation during ejection, Drug development and industrial pharmacy 36 (8) (2010) 972–979.

[16] V. Mazel, V. Busignies, H. Diarra, P. Tchoreloff, Lamination of pharmaceutical tablets due to air entrapment: direct visualization and influence of the compact thickness, International journal of pharmaceutics 478 (2) (2015) 702–704.

[17] V. Mazel, P. Tchoreloff, Lamination of pharmaceutical tablets: classification and influence of process parameters, Journal of Pharmaceutical Sciences 111 (5) (2022) 1480–1485.

[18] J. Meynard, F. Amado-Becker, P. Tchoreloff, V. Mazel, On the complexity

of predicting tablet capping, International Journal of Pharmaceutics 623 (2022) 121949.

[19] C. Martin, D. Bouvard, S. Shima, Study of particle rearrangement during powder compaction by the discrete element method, Journal of the Mechanics and Physics of Solids 51 (4) (2003) 667–693.

[20] M. A. Cooper, J. T. Clemmer, M. S. Oliver, D. S. Bolintineanu, J. B. Lechman, Visualization and simulation of particle rearrangement and deformation during powder compaction, in: Thermomechanics & Infrared Imaging, Inverse Problem Methodologies and Mechanics of Additive & Advanced Manufactured Materials, Volume 7: Proceedings of the 2020 Annual Conference on Experimental and Applied Mechanics, Springer, 2021, pp. 1–8.

[21] I. Boudina, E. Rondet, S. Nezamabadi, T. Sharkawi, Insight into tableted pellets by combining x-ray micro-computed tomography and experimental compaction, Powder Technology 397 (2022) 117083.

[22] C.-Y. Wu, S. M. Best, A. C. Bentham, B. C. Hancock, W. Bonfield, Predicting the tensile strength of compacted multi-component mixtures of pharmaceutical powders, Pharmaceutical research 23 (2006) 1898–1905.

[23] Y. Guo, C.-Y. Wu, C. Thornton, The effects of air and particle density difference on segregation of powder mixtures during die filling, Chemical Engineering Science 66 (4) (2011) 661–673.

[24] W. R. Mitchell, L. Forny, T. Althaus, D. Dopfer, G. Niederreiter, S. Palzer, Compaction of food powders: The influence of material properties and process parameters on product structure, strength, and dissolution, Chemical Engineering Science 167 (2017) 29–41.

[25] J.-F. Jerier, B. Hathong, V. Richefeu, B. Chareyre, D. Imbault, F.-V. Donze, P. Doremus, Study of cold powder compaction by using the discrete element method, Powder Technology 208 (2) (2011) 537–541.

[26] A. Mazor, L. Orefice, A. Michrafy, A. De Ryck, J. G. Khinast, A combined dem & fem approach for modelling roll compaction process, Powder Technology 337 (2018) 3–16.

[27] C. Gu, M. Kim, L. Anand, Constitutive equations for metal powders: application to powder forming processes, International Journal of Plasticity 17 (2) (2001) 147–209.

[28] A. Khoei, S. Keshavarz, A. Khaloo, Modeling of large deformation frictional contact in powder compaction processes, Applied Mathematical Modelling 32 (5) (2008) 775–801.

[29] H. Diarra, V. Mazel, V. Busignies, P. Tchoreloff, Fem simulation of the die compaction of pharmaceutical products: Influence of visco-elastic phenomena and comparison with experiments, International Journal of Pharmaceutics 453 (2) (2013) 389–394.

[30] S. Garner, E. Ruiz, J. Strong, A. Zavaliangos, Mechanisms of crack formation in die compacted powders during unloading and ejection: An experimental and modeling comparison between standard straight and tapered dies, Powder technology 264 (2014) 114–127.

[31] D. L. van der Haven, F. H. Ørtoft, K. Naelapää, I. S. Fragkopoulos, J. A. Elliott, Predictive modelling of powder compaction for binary mixtures using the finite element method, Powder Technology 403 (2022) 117381.

[32] I. Partheniadis, V. Terzi, I. Nikolakakis, Finite element analysis and modeling in pharmaceutical tableting, Pharmaceutics 14 (3) (2022) 673.

[33] D. Gethin, R. Ransing, R. Lewis, M. Dutko, A. Crook, Numerical comparison of a deformable discrete element model and an equivalent continuum analysis for the compaction of ductile porous material, Computers & Structures 79 (13) (2001) 1287–1294.

[34] A. Demirtas, G. R. Klinzing, Understanding die compaction of hollow spheres using the multi-particle finite element method (mpfem), Powder Technology 391 (2021) 34–45.

[35] P. Han, X. An, Y. Zhang, F. Huang, T. Yang, H. Fu, X. Yang, Z. Zou, Particulate scale mpfem modeling on compaction of fe and al composite powders, Powder Technology 314 (2017) 69–77.

[36] N. Audry, B. Harthong, D. Imbault, The mesoscale mechanics of compacted ductile powders under shear and tensile loads, Journal of the Mechanics and Physics of Solids (2024) 105807.

[37] N. Audry, B. Harthong, D. Imbault, Numerical modelling of contact adhesion in a random assembly of elastic–plastic particles, International Journal of Solids and Structures 295 (2024) 112826.

[38] B. Harthong, J.-F. Jérier, P. Dorémus, D. Imbault, F.-V. Donzé, Modeling of high-density compaction of granular materials by the discrete element method, International Journal of Solids and Structures 46 (18-19) (2009) 3357–3364.

[39] I. Schmidt, T. Kraft, H. Riedel, Tools for improving pm: Numerical homogenisation of elasto-plastic granule assemblies using discretised particles, in: European Congress and Exhibition on Powder Metallurgy. European PM Conference Proceedings, Vol. 3, The European Powder Metallurgy Association, 2008, p. 169.

[40] N. Abdelmoula, B. Harthong, D. Imbault, P. Dorémus, A study on the uniqueness of the plastic flow direction for granular assemblies of ductile particles using discrete finite-element simulations, Journal of the Mechanics and Physics of Solids 109 (2017) 142–159.

[41] P. A. Cundall, O. D. Strack, A discrete numerical model for granular assemblies, geotechnique 29 (1) (1979) 47–65.

[42] A. Russell, J. Strong, S. Garner, W. Ketterhagen, M. Long, M. Capece, Direct compaction drug product process modeling, AAPS PharmSciTech 23 (1) (2022) 67.

[43] K. L. Johnson, The correlation of indentation experiments, Journal of the Mechanics and Physics of Solids 18 (2) (1970) 115–126.

[44] L. Kogut, I. Etsion, Elastic-plastic contact analysis of a sphere and a rigid flat, J. Appl. Mech. 69 (5) (2002) 657–662.

[45] C. Tsigginos, J. Strong, A. Zavaliangos, On the force–displacement law of contacts between spheres pressed to high relative densities, International Journal of Solids and Structures 60 (2015) 17–27.

[46] V. L. Popov, M. Heß, Methode der Dimensionsreduktion in Kontaktmechanik und Reibung, Springer, 2013.

[47] V. L. Popov, M. Heß, Method of dimensionality reduction in contact mechanics and friction, Springer, 2015.

[48] K. L. Johnson, K. Kendall, A. D. Roberts, Surface energy and the contact of elastic solids, Proceedings of the royal society of London. A. mathematical and physical sciences 324 (1558) (1971) 301–313.

[49] L. Verlet, Computer" experiments" on classical fluids. i. thermodynamical properties of lennard-jones molecules, Physical review 159 (1) (1967) 98.

[50] B. Quentrec, C. Brot, New method for searching for neighbors in molecular dynamics computations, Journal of Computational Physics 13 (3) (1973) 430–432.

[51] T. Shire, K. J. Hanley, K. Stratford, Dem simulations of polydisperse media: efficient contact detection applied to investigate the quasi-static limit, Computational Particle Mechanics 8 (4) (2021) 653–663.

[52] B. Harthong, D. Imbault, P. Dorémus, The study of relations between loading history and yield surfaces in powder materials using discrete finite element simulations, Journal of the Mechanics and Physics of Solids 60 (4) (2012) 784–801.

[53] G. Gustafsson, H.-Å. Häggblad, P. Jonsén, Multi-particle finite element modelling of the compression of iron ore pellets with statistically distributed geometric and material data, Powder Technology 239 (2013) 231–238.

[54] P. Loidolt, M. H. Ulz, J. Khinast, Modeling yield properties of compacted powder using a multi-particle finite element model with cohesive contacts, Powder Technology 336 (2018) 426–440.

[55] J. Li, P. Han, Y. Xu, K. Liu, G. Zhang, P. Xu, A study of compaction densification behavior of composite particles by multiparticle finite element method, Mathematical Problems in Engineering 2022 (1) (2022) 8580849.

[56] S. Luding, Cohesive, frictional powders: contact models for tension, Granular matter 10 (4) (2008) 235–246.

[57] J. Ai, J.-F. Chen, J. M. Rotter, J. Y. Ooi, Assessment of rolling resistance models in discrete element simulations, Powder Technology 206 (3) (2011) 269–282.

[58] V. Mazel, V. Busignies, H. Diarra, P. Tchoreloff, Measurements of elastic moduli of pharmaceutical compacts: a new methodology using double compaction on a compaction simulator, Journal of pharmaceutical sciences 101 (6) (2012) 2220–2228.

[59] R. Roberts, R. Rowe, Determination of the critical stress intensity factor (kic) of microcrystalline cellulose using radially edge-cracked tablets, International journal of pharmaceutics 52 (3) (1989) 213–219.

[60] M. F. Ashby, H. Shercliff, D. Cebon, Materials: engineering, science, processing and design, Butterworth-Heinemann, 2018.

[61] P. A. Thomas, J. D. Bray, Capturing nonspherical shape of granular media with disk clusters, Journal of Geotechnical and Geoenvironmental Engineering 125 (3) (1999) 169–178.

[62] F. Da Cruz, S. Emam, M. Prochnow, J.-N. Roux, F. Chevoir, Rheophysics of dense granular materials: Discrete simulation of plane shear flows, Physical Review E 72 (2) (2005) 021309.

[63] K. Kamrin, G. Koval, Nonlocal constitutive relation for steady granular

flow, Physical review letters 108 (17) (2012) 178301.

[64] S. Chialvo, J. Sun, S. Sundaresan, Bridging the rheology of granular flows in three regimes, Physical review E 85 (2) (2012) 021305.

[65] C. S. Giménez, B. Finke, C. Schilde, L. Froböse, A. Kwade, Numerical simulation of the behavior of lithium-ion battery electrodes during the calendaring process via the discrete element method, Powder Technology 349 (2019) 1–11.

[66] R. Ge, D. J. Cumming, R. M. Smith, Discrete element method (dem) analysis of lithium ion battery electrode structures from x-ray tomography-the effect of calendering conditions, Powder Technology 403 (2022) 117366.

[67] M. Sonzogni, J.-M. Vanson, Y. Reynier, S. Martinet, K. Ioannidou, F. Radjai, Discrete modeling of the calendering process for positive electrodes of li-ion batteries, Powder Technology 442 (2024) 119891.

[68] N. Moshtagh, Minimum volume enclosing ellipsoid, `MATLAB Central File Exchange`, `https://www.mathworks.com/matlabcentral/fileexchange/9542-minimum-volume-enclosing-ellipsoid` (February 2025).